

Falling plates with leading-edge vortex shedding

Yu Jun Loo¹ and Silas Alben¹

¹*Department of Mathematics, University of Michigan, Ann Arbor, MI 48109, USA*

Abstract

We develop a new numerical method for thin plates falling in inviscid fluid that allows for leading-edge vortex shedding. The inclusion of leading-edge shedding restores physical dynamics to vortex-sheet models of falling bodies, and for the first time large-amplitude fluttering and tumbling are observed in inviscid simulations. Leading-edge shedding is achieved by introducing a novel quadrature rule and smoothing procedure for the Birkhoff-Rott equations. The smoothing error is controlled by a novel fencing procedure. We find a transition point between fluttering and tumbling that is consistent with previous viscous simulations and experiments, and other falling motions such as looping, autorotation are also observed as the plate density increases. The dipole street wakes behind the fluttering plates resemble those in experiments. We consider plates bent into V shapes and study the effects of density and bending angle on the qualitative falling dynamics. At small densities, increasing the bending angle stabilizes the falling motion into fluttering, while at large densities, decreasing the bending angle stabilizes the falling motion into autorotation. In the autorotation regime, the magnitude of angular velocity increases as time cubed before it reaches a terminal angular velocity, and in the fluttering regime, the fluttering frequency scales as the $-1/2$ power of R_1 , the plate density.

1 Introduction

Among the simplest examples of fluid-structure interaction is a body falling freely through fluid, driven only by gravity. It is a simple system that shows many of the complex dynamics that occur in fluid-structure interactions in the natural environment. The physical mechanisms involved in passive falling dynamics at high Reynolds numbers are relevant to the settling of dandelion seeds [Cum+18] and the passive gliding of swifts [TT01], for example. The underlying passive dynamics of these systems has inspired energy-efficient designs for microscale gliders [Kim+21].

For macroscopic falling objects, the Reynolds number $\gtrsim 10^2$ [Cum+18] [APW05b] [Tam+10]. The numerical resolution required for Navier-Stokes simulations of these problems at high Reynolds numbers can make investigation of the long-time dynamics across parameter spaces prohibitively expensive. Recently, several authors have developed less expensive inviscid vortex-shedding models as approximations to these high-Reynolds-number systems, for both rigid [JS05] [ML09] [Soh24] and flexible falling bodies [Alb10a].

In the numerical model used in [Alb10a], the release of vorticity from a body edge is halted intermittently whenever the fluid velocity at the edge is directed onto the body, in order to avoid numerical issues associated with leading-edge shedding. This approach was also used by [Hua+18] and [Soh24], for hovering and falling bodies respectively. Stopping the shedding of vorticity at the leading edge leads to a concentrated vortex attached to the leading edge, but in most situations, vorticity is continually shed from the leading edge, which dramatically changes the pressure loading on the body. Previously, [Pan+12] found that including leading-edge shedding greatly improved the accuracy of thrust forces in an inviscid boundary element model of flow past a flapping foil.

In the aforementioned inviscid models without leading-edge shedding, many of the dynamics that are commonly observed in both experiments and direct Navier-Stokes simulations of falling bodies, such as tumbling and side-to-side fluttering, fail to occur. Instead, the models settle into long periods of gliding and diving where the body moves nearly tangentially to its leading edge. In this work, we will demonstrate a robust method for continual leading-edge shedding that results in more realistic dynamics. A related body of work has developed the concept of a leading-edge suction parameter (LESP) to determine when leading-edge shedding occurs [Ram+12] [Nar+23] and has employed it in discrete vortex models similar to the one used in this study. With this approach, shedding is still halted intermittently (but less frequently than in [Alb10a]), and when shedding occurs the vortex sheet is discontinuous across the leading edge [Ram+12] [Eld19, p. 182].

In this study, we propose a series of improvements to the numerical scheme described in [Alb09]. These improvements stabilize the interaction between the falling body and the vortex sheet shed from the leading edge, allowing for continual shedding from the leading edge. To demonstrate the method, we use it to study the long-time behavior of falling plates, both flat and curved, in an inviscid fluid. With leading-edge shedding present, both fluttering and periodic tumbling are observed for the first time in inviscid simulations.

In the experiments of [Fie+97] on falling disks, the motions were classified as either steady falling, periodic fluttering, tumbling, or chaotic motions. At the high Reynolds number $\sim 10^3$ relevant to this study, we do not find steady falling (with constant orientation). The first systematic study of falling plates was given by [Smi71]. There, the plate dynamics were classified by the dimensionless moment of inertia I^* . For small values of I^* , the plates flutter side to side. As I^* increases, the plate dynamics transition to a tumbling

motion where the plate falls end-over-end. There, the transition region between fluttering and tumbling was found to be $0.2 < I^* < 0.3$, for thickness to length ratios in the range $[1/4, 2/5]$. This transition region was further verified by both the direct Navier-Stokes simulations of [Wan+16] who determined it as $0.21 < I^* < 0.31$ for thickness to length ratios $[1/20, 1/4]$, as well as the inviscid simulations of [Soh24] who determined the transition point as $I^* \approx 0.27$ for a plate of zero thickness. According to the bifurcation diagram in [Xia+18], the transition between fluttering and tumbling occurs at $I^* \approx 0.2$ for thickness to length ratios in the range $[1/200, 3/80]$. The experiments of [BEM98] classified falling plates by the square of the dimensionless mass density Fr and showed for the range of thickness to length ratios $[1/320, 1/5]$, that the transition from fluttering to tumbling occurs at $\text{Fr}_c = 0.67 \pm 0.05$, or $I^* \approx 0.4$, slightly higher than the aforementioned studies suggest. These experimental results were reproduced numerically in [RKD20] which determined the transition region to be $0.24 < I^* < 0.4$ for the thickness to length ratios $[1/14, 1/5]$, and attributes the difference in transition regions from [Wan+16] to the sensitivity of the system to initial conditions. On the other hand, [Soh24] suggests that the differences may be due to the experimental set up. The simulations in [Wan+16] suggest that decreasing the thickness to length ratio lowers the transition point, shifting the transition region downward. In this study, we consider plates of zero thickness.

Many other recent works have studied rounded bodies falling in a fluid. Direct Navier-Stokes simulations of falling thin ellipses were performed in [PW04] [APW05b] [APW05a] [WL15]. In [WL15], the ellipses were classified based on their dimensionless moment of inertia I^* , and their aspect ratio. The effects of both I^* and the Reynolds number Re on the resulting dynamics was studied. Near the transition between fluttering and tumbling, $0.12 < I^* < 0.35$, chaotic motions appeared where the ellipse alternated between fluttering and tumbling at irregular intervals. For falling circular disks, decreasing I^* (or Fr) introduces 3D effects. The side-to-side fluttering motion transitions smoothly to an elliptical then circular spiraling motion [ZCL11]. In the present study, we will classify the motions across $R_1 = \text{Fr}^2$, the dimensionless mass density of the plates, which is equivalent to $I^* \approx \frac{4}{3\pi}R_1$ [Soh24].

Multiple falling plates were studied in [KD20]. [HNK14] studied the phase space of fluttering and tumbling motions of falling coins and obtained statistics for the coins' landing positions. In [Cum+18], the separated wake behind a dandelion seed induced by its porous structure was observed. Effects of porosity and flexibility on the dynamics of falling thin objects were studied by [Led+19] and [Tam+10] respectively. In [Led+19], the role of porosity in stabilizing the passive fluttering motion of a falling dandelion seed was studied. A related stabilization is caused by holes in a falling coin, studied by [VSK16].

[JS05] presented some of the first inviscid simulations of a falling plate, using shed vortex sheets similar to the present study. [ML09] used a related inviscid model, the Brown-Michael method, with the vortex sheets replaced by point vortices whose strengths and positions evolve in time. These studies were confined to the period of initial growth of small perturbations from broadside-on falling ($t \lesssim 15$), before steady-state large-amplitude fluttering or tumbling occur. In the present study, we investigate the steady-state dynamics up to $t \approx 500$.

Several studies have compared inviscid models with viscous simulations and experiments. Remarkable agreement between dye-visualized shed vortex sheets in experiments [Did79] and inviscid computations were shown by [NK94] for a flow through a circular tube. Good agreement between experiments and inviscid simulations for the forces and flows around a flapping foil were shown by [Pan+12], as long as leading-edge shedding was accounted for. In [She+12], without leading-edge vortex shedding, there was less agreement between the forces computed with inviscid and direct Navier-Stokes methods, which could also be due to the absence of skin friction. In the present study we incorporate leading-edge shedding as well as skin friction effects.

2 Model

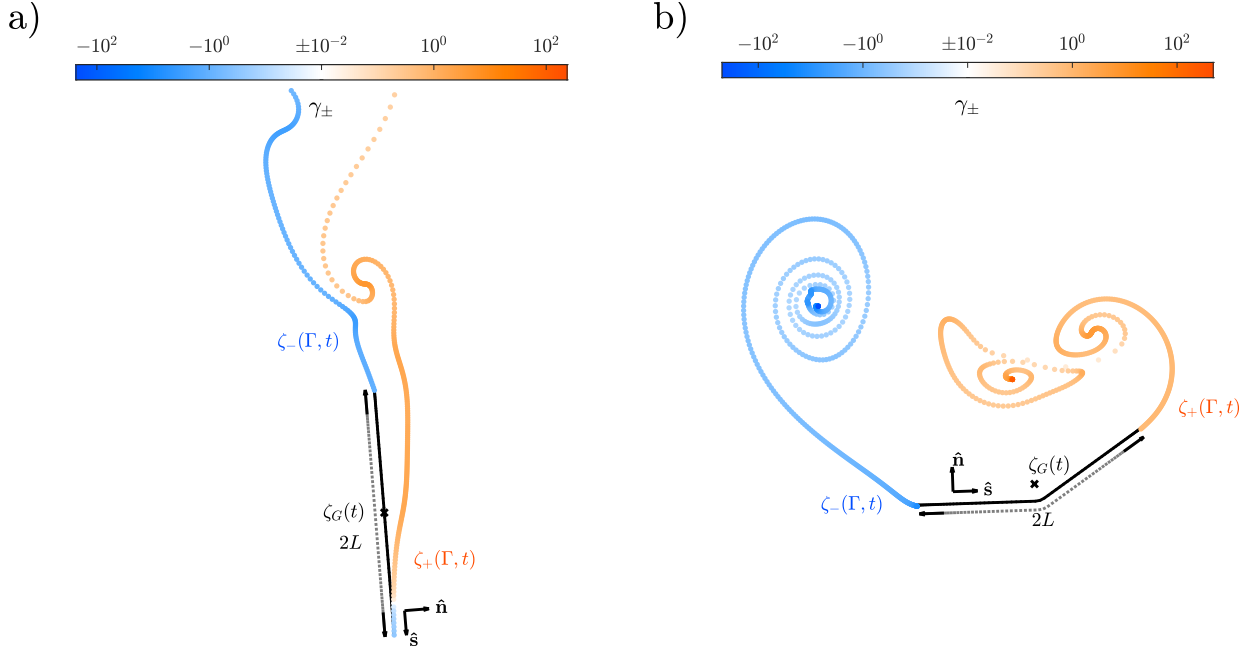


Figure 1: (a) A flat and (b) V-shaped plate falling under gravity, with center of mass ζ_G and length $2L$. It has unit tangent and normal vectors \hat{s} and \hat{n} respectively. Off the edges, vortex sheets are being shed with their strength γ_{\pm} colored with a logarithmic scale. They are parameterized by $\zeta_{\pm}(\Gamma, t)$ where Γ is the circulation.

Many previous works have studied falling flat plates [JS05] [BEM98] [Soh24] [PR24]. Here we study this case as well as the more general class of rigid V-shaped plates, with an example shown in figure 1. We have also considered other plate shapes but focus on V-shaped plates because they yield a wider range of dynamics. The plates are represented by a 1D curve in the 2D x - y fluid plane. Both the body and flow extend uniformly with width W in the z (out-of plane) direction. The body has length $2L$ in the x - y plane and thickness $h \ll L$. The thickness of the body is approximated as 0 relative to the characteristic length scale L . The x - y flow velocity is written as the complex function $u(z) + iv(z)$, where $z = x + iy$ and $i = \sqrt{-1}$. The body position is written as a complex-valued curve

$$\zeta(s, t) = \zeta_G(t) + \zeta_0(s)e^{i\beta(t)} \quad (1)$$

with $\zeta_G(t) = x_G(t) + iy_G(t)$ the center of mass, $\zeta_0(s)$ the mean-zero (smooth) shape of the body, fixed in time, and $\beta(t)$ the body's orientation angle, with initial value $\beta(0) = 0$. The arc length parameter $s \in [-L, L]$ along the body. The unit tangent vector along the body is $\hat{s} = \partial_s \zeta(s, t)$ and the unit normal is $\hat{n} = i\hat{s}$. We use + to denote the the side of the body towards which \hat{n} points and - for the other side. We also use + for the $s = L$ end of the body and - for the $s = -L$ end.

Note that the logarithmic scales in figure 1 (and several subsequent figures) are actually two logarithmic scales joined together, to show both signs of vortex-sheet strength γ . Points with small $|\gamma|$ ($\leq 10^{-2}$) are colored white.

2.1 Rigid-body equations

2.1.1 Force balance in an inviscid fluid

A local force balance on a small portion of the body lying in the interval $[s - \frac{\Delta s}{2}, s + \frac{\Delta s}{2}]$ gives

$$\rho_b h W \Delta s \partial_{tt} \zeta(s, t) = -W \Delta s [p]_+^+(s) \hat{n}(s) - i \rho_b h W \Delta s g + f_{int}. \quad (2)$$

The left side is the body inertia, with ρ_b the body mass per unit volume. The first term on the right side is the pressure force, with $[p]_+^+ = p^+ - p^-$ the jump in pressure across the body. The second term on the right side is the gravitational force, with g the gravitational acceleration. The third term on the right side, f_{int} , is the sum of the internal forces exerted on this portion of the body by the neighboring portions, in order to maintain the rigid shape of the body. Summing over the entire body on both sides of the equation and taking the limit $\Delta s \rightarrow 0$, we obtain the equation for the center-of-mass motion:

$$\rho_b h W 2L \partial_{tt} \zeta_G(t) = -W \int_{-L}^L [p]_+^+(s) \hat{n}(s) ds - i \rho_b h W 2L g. \quad (3)$$

The net contribution from the internal forces vanishes because they appear in equal and opposite pairs, by Newton's third law.

2.1.2 Nondimensionalization

To nondimensionalize the equations, we take the half-length of the body, L , as the characteristic length scale. We define the characteristic velocity U as an approximation of the body's terminal speed, its time-averaged

speed in the steady-state falling motion reached after the initial transient dynamics. At steady state the left side of (3) has time-average zero and the pressure and gravity terms on the right side balance. The high-Reynolds-number scaling of $[p]_+^+$ is $\rho_f U^2$, e.g. by considering the Bernoulli equation. Thus $\rho_f U^2 \sim \rho_b h g$ so we take $U = \sqrt{\frac{\rho_b h g}{\rho_f}}$ as the characteristic velocity scale. Choosing $\rho_f U^2$ for the characteristic pressure scale, we can now nondimensionalize the variables as follows:

$$t = \tilde{t} \frac{L}{U}, \quad \zeta_G = \tilde{\zeta}_G L, \quad [p]_+^+ = \tilde{[p]_+^+} \rho_f U^2, \quad s = \tilde{s} L. \quad (4)$$

Here, the variables with tildes, \tilde{t} , $\tilde{\zeta}$, $\tilde{[p]_+^+}$, \tilde{s} , denote their dimensionless counterparts. After substituting these variables into (3) and suppressing the tildes, we obtain the dimensionless force balance equation, essentially equivalent to the versions in [Alb10a] and [Soh24]:

$$R_1 \partial_{tt} \zeta_G(t) = -\frac{1}{2} \int_{-1}^1 [p]_+^+(s) \hat{\mathbf{n}}(s) ds - i. \quad (5)$$

Here, $R_1 = \frac{\rho_b h}{\rho_f L}$ is the dimensionless mass density of the body, and measures the importance of body inertia relative to fluid inertia. This quantity is equal to Fr , the dimensionless Froude number as defined in [Soh24] [JS05], and equal to Fr^2 as defined in [BEM98] and [RKD20].

2.1.3 Torque balance in an inviscid fluid

The angular momentum about the origin of the small portion of the body lying in the interval $[s - \frac{\Delta s}{2}, s + \frac{\Delta s}{2}]$ is

$$\mathbf{r} \times (m\mathbf{v}) = \zeta(s, t) \times \rho_b Wh \Delta s \partial_t \zeta(s, t) \quad (6)$$

where \times denotes the cross product, assuming the operands are mapped from complex scalars to 3-vectors, e.g. from $z = a + ib$ to $\mathbf{z} = (a, b, 0)^T$. Then the cross product of two complex scalars, $\mathbf{z}_1 \times \mathbf{z}_2$, is given by $-\Re(iz_1 \bar{z}_2)$. We set the time-rate-of-change of the angular momentum (6) equal to the torque about the origin exerted by the forces in (2):

$$\zeta(s, t) \times \rho_b Wh \Delta s \partial_{tt} \zeta(s, t) = \zeta(s, t) \times (-W \Delta s [p]_+^+(s) \hat{\mathbf{n}}(s) - i \rho_b h W \Delta s g + f_{int}) \quad (7)$$

We insert $\zeta(s, t)$ from (1) and sum (7) over the body, taking the limit $\Delta s \rightarrow 0$. The resulting integrals are simplified using (3) and that the facts that $\zeta_0(s)$ has s -mean zero and the internal forces exert no net torque on the body. We obtain

$$\rho_b Wh \int_{-L}^L |\zeta_0(s)|^2 ds \partial_{tt} \beta(t) = W \int_{-L}^L \Re \left(i \zeta_0(s) e^{i\beta(t)} \overline{([p]_+^+(s) \hat{\mathbf{n}}(s))} \right) ds. \quad (8)$$

Finally, by nondimensionalizing again as above we obtain

$$I_G \partial_{tt} \beta(t) = \int_{-1}^1 \Re \left(i \zeta_0(s) e^{i\beta(t)} \overline{([p]_+^+(s) \hat{\mathbf{n}}(s))} \right) ds. \quad (9)$$

Here, $I_G = R_1 \int_{-1}^1 |\zeta(s, t) - \zeta_G(s)|^2 ds = R_1 \int_{-1}^1 |\zeta_0(s)|^2 ds$ is the (dimensionless) moment of inertia of the body about its center of mass. Henceforth, all equations are dimensionless.

2.2 Fluid equations

In the presence of small viscosity, the fluid velocity matches the body velocity on its surface, but rapidly transitions to other values as one moves away from the body through thin boundary layers along the body surface. In the limit of zero viscosity, a boundary layer shrinks to a zero-thickness vortex sheet along the body surface, and the velocity tangent to the body surface jumps discontinuously across the vortex sheet. In the limit of zero body thickness, the vortex sheets on the two sides of the body coincide and are a single vortex sheet called the “bound” vortex sheet [Eld19].

With small viscosity, vorticity diffuses slightly from the boundary layers along the body but mainly enters the fluid at “separation points” where the boundary layer is advected into the flow, particularly at the sharp edges of the body. In our zero-viscosity model the situation is similar—there is no diffusion of vorticity from the vortex sheets, only advection from the separation points, which we assume to be located only at the two edges of the body. Consequently, two “free” vortex sheets emanate from the body, one from each edge. The bound vortex sheet along the body and the free vortex sheets form one continuous vortex sheet (discretized in figure 1), which we compute at each time step.

The body and flow are initially at rest with zero vorticity. As t increases from 0, gravity causes the body to accelerate with a downward component. As the body moves there is a corresponding fluid motion that can be represented in terms of the strengths and positions of the bound and free vortex sheets. As time increases, the lengths of the free vortex sheets increase at each edge, starting from zero. The bound vortex sheet position is the same as the body, $\zeta(s, t)$, $-1 \leq s \leq 1$. The free vortex sheets emanating from the $s = \pm 1$ edges are denoted $\zeta_+(s, t)$, $s \in [1, s_+ + 1]$ and $\zeta_-(s, t)$, $s \in [-s_- - 1, -1]$. Here, s_\pm are the lengths of the positive and negative vortex sheets respectively, and the vortex sheet strengths $\gamma_\pm(s, t)$ are defined analogously.

The strength of the entire (bound and free) vortex sheet is denoted $\gamma(s, t)$, with $s \in [-1 - s_-, 1 + s_+]$. We denote the restriction of $\gamma(s, t)$ to the negative, positive, and bound vortex sheets as $\gamma_-(s, t)$, $\gamma_+(s, t)$, and $\gamma_b(s, t)$ respectively.

Integrating the vortex strengths γ_b , and γ_\pm against the Biot-Savart kernel, we obtain an equation for the conjugate fluid velocity $w(z) = u(z) - iv(z)$,

$$u(z) - iv(z) = \frac{1}{2\pi i} \int_{-1}^1 \frac{\gamma_b(s, t)}{z - \zeta(s, t)} ds + \frac{1}{2\pi i} \int_{-s_- - 1}^{-1} \frac{\gamma_-(s, t)}{z - \zeta_-(s, t)} ds + \frac{1}{2\pi i} \int_1^{s_+ + 1} \frac{\gamma_+(s, t)}{z - \zeta_+(s, t)} ds. \quad (10)$$

Let $\Gamma(s, t)$ denote the arc length integral of γ along the positive and negative vortex sheets, defined piecewise:

$$\Gamma(s, t) = \begin{cases} \int_{-s_- - 1}^s \gamma(s', t) ds', & s \in [-s_- - 1, -1] \\ \int_1^s \gamma_+(s', t) ds', & s \in [1, 1 + s_+] \end{cases} \quad (11)$$

and $\Gamma_\pm(t)$ denote the total circulations in the positive and negative vortex sheets, i.e.

$$\Gamma_+(t) \equiv \int_1^{1+s_+} \gamma_+(s, t) ds \quad ; \quad \Gamma_-(t) \equiv \int_{-s_- - 1}^{-1} \gamma_-(s, t) ds. \quad (12)$$

Then, by reparameterizing the positions of the free vortex sheets in terms of Γ , we may rewrite the equation for the conjugate velocity as

$$u(z) - iv(z) = \frac{1}{2\pi i} \int_{-1}^1 \frac{\gamma_b(s, t)}{z - \zeta(s, t)} ds + \frac{1}{2\pi i} \int_0^{\Gamma_-(t)} \frac{d\Gamma}{z - \zeta_-(\Gamma, t)} + \frac{1}{2\pi i} \int_0^{\Gamma_+(t)} \frac{d\Gamma}{z - \zeta_+(\Gamma, t)}. \quad (13)$$

Note that $\Gamma_+(t)$ is the negative of the quantity with this name in [Jon03; Alb09] and $\Gamma(s, t)$ differs from the quantity with the same name in those works by an additive constant ($\Gamma_+(t)$) on the positive vortex sheet.

2.2.1 Birkhoff-Rott equation

By demanding that the pressure be a continuous field across the free vortex sheets, the free vortex sheets must evolve with velocities equal to the average of the fluid velocities across their surfaces [Eld19, p. 84]. A consequence of the Sokhotski–Plemelj formulae is that the principal value of a singular integral is the average of its limiting values on either side. A brief discussion of this formula is included in appendix A. Hence, by evaluating (13) on the free sheets in the principle-value sense, we obtain the following Birkhoff-Rott equations for the (conjugate) fluid velocity of the free sheets.

$$\begin{aligned} \partial_t \bar{\zeta}_\pm(\Gamma, t) = & \frac{1}{2\pi i} \int_{-1}^1 \frac{\gamma_b(s, t)}{\zeta_\pm(\Gamma, t) - \zeta(s, t)} ds + \frac{1}{2\pi i} \int_0^{\Gamma_-(t)} \frac{d\Gamma'}{\zeta_\pm(\Gamma, t) - \zeta_-(\Gamma', t)} \\ & + \frac{1}{2\pi i} \int_0^{\Gamma_+(t)} \frac{d\Gamma'}{\zeta_\pm(\Gamma, t) - \zeta_+(\Gamma', t)}. \end{aligned} \quad (14)$$

For the computational method, we will modify the Birkhoff-Rott equations as described in section 3.3.2.

2.2.2 Blob regularization

The Birkhoff-Rott equations for the evolution of the free vortex sheets are ill-posed, and develop a curvature singularity at a finite critical time [Moo79] [Kra86a] [She92]. Krasny showed that the Birkhoff-Rott equations can be evolved numerically past the critical time by introducing a smoothing parameter δ to “desingularize” the equations [Kra86b]:

$$\begin{aligned} u(z) - iv(z) = & \frac{1}{2\pi i} \int_{-1}^1 \frac{\gamma_b(s, t)}{z - \zeta(s, t)} ds + \frac{1}{2\pi i} \int_0^{\Gamma_-(t)} \frac{\overline{z - \zeta_-(\Gamma', t)}}{|z - \zeta_-(\Gamma', t)|^2 + \delta^2} d\Gamma' \\ & + \frac{1}{2\pi i} \int_0^{\Gamma_+(t)} \frac{\overline{z - \zeta_+(\Gamma', t)}}{|z - \zeta_+(\Gamma', t)|^2 + \delta^2} d\Gamma'. \end{aligned} \quad (15)$$

The presence of δ smooths the kernel into a vortex blob, with core size determined by δ [Kra90]. Here, and in all that follows, we take $\delta = 0.2$ as is done in [NK94].

2.2.3 No-penetration condition & Kelvin’s circulation theorem

Let the body velocity $\partial_t \zeta(s, t)$ have tangential and normal components τ and ν respectively:

$$\partial_t \zeta(s, t) = \tau(s, t) \hat{\mathbf{s}}(s, t) + \nu(s, t) \hat{\mathbf{n}}(s, t). \quad (16)$$

Taking the limit that z approaches the body in (15), analogous to (14) we have

$$\begin{aligned} \mu(s, t) \hat{\mathbf{s}}(s, t) + \xi(s, t) \hat{\mathbf{n}}(s, t) = & \frac{1}{2\pi i} \int_{-1}^1 \frac{\gamma_b(s', t)}{\zeta(s, t) - \zeta(s', t)} ds' + \frac{1}{2\pi i} \int_0^{\Gamma_-(t)} \frac{\overline{\zeta(s, t) - \zeta_-(\Gamma, t)}}{|\zeta(s, t) - \zeta_-(\Gamma, t)|^2 + \delta^2} d\Gamma \\ & + \frac{1}{2\pi i} \int_0^{\Gamma_+(t)} \frac{\overline{\zeta(s, t) - \zeta_+(\Gamma, t)}}{|\zeta(s, t) - \zeta_+(\Gamma, t)|^2 + \delta^2} d\Gamma. \end{aligned} \quad (17)$$

Here, μ and ξ are the averages of the tangential and normal velocities on the two sides of the body. The no-penetration condition states that the fluid and body velocities have the same components normal to the body at the the body surface:

$$\nu(s, t) = \xi(s, t). \quad (18)$$

That is,

$$\Re(\hat{\mathbf{n}}(s, t) \partial_t \zeta(s, t)) = \Re \left(\hat{\mathbf{n}}(s, t) \left(\frac{1}{2\pi i} \int_{-1}^1 \frac{\gamma_b(s', t)}{\zeta(s, t) - \zeta(s', t)} ds' + \frac{1}{2\pi i} \int_0^{\Gamma_-(t)} \frac{\overline{\zeta(s, t) - \zeta_-(\Gamma, t)}}{|\zeta(s, t) - \zeta_-(\Gamma, t)|^2 + \delta^2} d\Gamma \right. \right. \\ \left. \left. + \frac{1}{2\pi i} \int_0^{\Gamma_+(t)} \frac{\overline{\zeta(s, t) - \zeta_+(\Gamma, t)}}{|\zeta(s, t) - \zeta_+(\Gamma, t)|^2 + \delta^2} d\Gamma \right) \right), \quad (19)$$

(Note that in complex notation, the dot product of two vectors $\mathbf{z}_1 \cdot \mathbf{z}_2$ is given by $\Re(\overline{z_1} z_2)$.) Given known positive and negative circulations, the no-penetration condition (19) uniquely determines γ_b provided we add the additional constraint that the total circulation in the fluid vanishes [Gol90] [Eld19, p. 285]. Indeed, since the body is released from rest, the initial circulation present in fluid is zero. Combined with Kelvin's circulation theorem, which asserts that the total circulation is independent of time [Eld19, p. 36], we must have

$$\Gamma_+(t) + \Gamma_-(t) + \Gamma_b(t) = 0. \quad (20)$$

Here, $\Gamma_b(t) = \int_{-1}^1 \gamma_b(s, t) ds$ is the total circulation on the body. Alongside the no-penetration condition (19), this is an additional constraint that must be satisfied by the bound vortex strength γ_b .

2.3 Pressure-jump equation

By considering the Bernoulli equation in the reference frame of the moving body, and taking its difference when evaluated on both sides of the body, the following pressure-jump equation can be obtained [Eld19, p. 85] [Alb12].

$$[p]_+^+(s, t) = \partial_t(\Gamma_-(t) + \Gamma_b(s, t)) + (\mu(s, t) - \tau(s, t))\gamma_b(s, t) \quad (21)$$

Here, $\Gamma_b(s, t) = \int_{-1}^s \gamma_b(s, t) ds$, and $\mu(s, t)$ is the $\hat{\mathbf{s}}$ component of (17).

The equation for the pressure jump (21) is identical to that in [HNK16] and [Soh24]. However, we note that there is another, equally natural choice for the pressure-jump equation:

$$\begin{cases} \partial_s [p]_+^+(s, t) = \partial_t \gamma_b(s, t) + \partial_s((\mu(s, t) - \tau(s, t))\gamma_b(s, t)), \\ [p]_+^+(-1, t) = 0 \end{cases} \quad (22)$$

This equation was used with success in [Alb10a] and [MA20], and can be obtained for instance, by differentiating (21) with respect to arc length. The edge condition follows from the Birkhoff-Rott equations which demand that the pressure jump across the free sheet vanishes [Eld19]. Hence, by the continuity of the pressure jump from the body to free sheets, $[p]_+^+(\pm 1, t) = 0$. The two equations (21) and (22) are therefore equivalent provided that the constraint

$$\partial_t \Gamma_-(t) + (\mu(-1, t) - \tau(-1, t))\gamma_b(-1, t) = 0 \quad (23)$$

is satisfied. However, the situation is complicated by the fact that in a numerical implementation, the quantities $\partial_t \Gamma_-(t) + (\mu(\pm 1, t) - \tau(\pm 1, t))\gamma_b(\pm 1, t)$ may cease to be zero, leading to different approximate formulations of the pressure equation. Indeed, although both pressure equations are equivalent in a mathematical sense, they become distinct with the blob regularization of the singular integrals in (19), as discussed next.

2.4 Kutta condition

The system of equations (5), (9), (14), and (19)–(21) contains two functions that are as yet undetermined: $\Gamma_-(t)$ and $\Gamma_+(t)$, the cumulative circulations released at each edge. They are determined at each time t by the Kutta condition, the physical constraint that the flow velocity be bounded at the sharp edges of the body. In the seminal work [Jon03], Jones shows that the bounded velocity constraint has multiple formulations that are mathematically equivalent:

$$\begin{cases} \partial_t \Gamma_-(t) + (\mu(-1, t) - \tau(-1, t))\gamma_b(-1, t) = 0, \\ \partial_t \Gamma_+(t) - (\mu(1, t) - \tau(1, t))\gamma_b(1, t) = 0 \end{cases} \quad (24)$$

$$\begin{cases} \gamma_b(-1, t) = \gamma_-(1, t), \\ \gamma_b(1, t) = \gamma_+(1, t) \end{cases} \quad (25)$$

$$\begin{cases} \sigma(-1, t) = 0, & \gamma_b(s, t) = \frac{\sigma(s, t)}{\sqrt{1-s^2}} \\ \sigma(1, t) = 0, & \end{cases} \quad (26)$$

Here, $\sigma(\pm 1, t)$ is the “suction parameter” at the \pm edge [Eld19, p. 178]. It can be shown that the generic solution to (19) γ_b has inverse square root singularities and is thus of the form $\gamma_b(s, t) = \frac{\sigma(s, t)}{\sqrt{1-s^2}}$ for some continuous $\sigma(s, t)$ [Mus58]. (26) is therefore equivalent to removing the singularities and leaving γ_b finite at the edges. In [Jon03], it is shown using explicit formulae for γ_b that enforcing the constraints (24) is

equivalent to removing these singularities. Hence both Kutta conditions (24) and (26) are equivalent. Furthermore, as shown in section 2.3, (24) is really the assertion that the pressure jump is continuous from the body to the free vortex sheet. (25) asserts that the vortex sheet strength is continuous from the body to the free vortex sheet. Since a version of (21) holds for the entire vortex sheet (both free and bound parts), in general the pressure jump $[p]^\pm$ is continuous if and only if the vortex strength γ is continuous. Hence, mathematically speaking, equations (24)–(26) are all equivalent, and can be viewed as “the” Kutta condition.

However, with a nonzero blob regularization δ of the free sheets but not the bound sheet in (19), (24)–(26) become three distinct conditions. In the standard vortex shedding method used in previous studies, including those from the present authors, exactly one point is released onto the free sheets at each time step. The value of the circulation at this newly released point is chosen so that the computed solution satisfies one of (24)–(26). An alternative method that we have implemented is satisfying more than one of (24)–(26) simultaneously at each time step, by releasing the corresponding number of vortex sheet points from each edge. Such a method is only possible because these equations are nonequivalent. However, the careful investigation of such methods is beyond the scope of this paper.

Based on experimentation, we have selected (26) as the Kutta condition for the present study because it seems to be the most numerically stable.

There is another Kutta condition, distinct from (24)–(26), that has also been used (e.g. [Jon03; Soh24]):

$$\begin{cases} \gamma_b(-1, t) = 0, \\ \gamma_b(1, t) = 0. \end{cases} \quad (27)$$

Unlike (24)–(26), this Kutta condition applies the principle of bounded velocity not to the original, singular equations, but to the blob-regularized equations. This Kutta condition is strictly stronger than (26), since if the bound circulation γ_b is to attain a finite value at the edges of the body, the suction must vanish there as well. It suppresses not only the intrinsic inverse square root singularities that arise in the general solution of γ_b , but also logarithmic singularities that arise by blob regularizing only the free, not bound, sheets. To explain the logarithmic singularities, let us fix t for the moment and suppose for simplicity that our plate is flat and parameterized by $\zeta(s, t) = s$, $-1 < s < 1$. Then, as noted in [Jon03], and [Mus58, p. 42], we may write the plate’s contribution to the (conjugate) fluid velocity as

$$\begin{aligned} \frac{1}{2\pi i} \int_{-1}^1 \frac{\gamma_b(s, t)}{z - \zeta(s, t)} ds &= \frac{1}{2\pi i} \int_{-1}^1 \frac{\gamma_b(s, t) - \gamma_b(\pm 1, t)}{z - s} ds + \frac{1}{2\pi i} \gamma_b(\pm 1, t) \int_{-1}^1 \frac{ds}{z - s} \\ &= \frac{\gamma_b(\pm 1, t)}{2\pi i} \log\left(\frac{z+1}{z-1}\right) + \Phi_\pm(z) \end{aligned}$$

Here, $\Phi_\pm(z) = \frac{1}{2\pi i} \int_{-1}^1 \frac{\gamma_b(s, t) - \gamma_b(\pm 1, t)}{z - s} ds$ is a bounded function near the \pm edge. This is because the numerator of the integrand vanishes at the \pm edge, canceling the singularity there. A justification of this subtle point in a more general case is included in appendix A. Thus when (15) is used to compute the fluid velocity with one of (24)–(26), logarithmic singularities occur at the edges of the body where γ_b is nonzero. This is because although the singular integrals in (13)

$$\begin{aligned} \frac{1}{2\pi i} \int_{-s_- - 1}^{-1} \frac{\gamma_-(s, t)}{z - \zeta_-(s, t)} ds &= \frac{1}{2\pi i} \int_0^{\Gamma_-(t)} \frac{d\Gamma'}{z - \zeta_-(\Gamma', t)}, \\ \frac{1}{2\pi i} \int_1^{1+s_+} \frac{\gamma_+(s, t)}{z - \zeta_+(s, t)} ds &= \frac{1}{2\pi i} \int_0^{\Gamma_+(t)} \frac{d\Gamma'}{z - \zeta_+(\Gamma', t)} \end{aligned} \quad (28)$$

likewise have logarithmic singularities at the edges of the body that cancel those of the plate, their blob regularized counterparts in (15),

$$\frac{1}{2\pi i} \int_0^{\Gamma_-(t)} \frac{\overline{z - \zeta_-(\Gamma, t)}}{|z - \zeta_-(\Gamma, t)|^2 + \delta^2} d\Gamma, \quad \frac{1}{2\pi i} \int_0^{\Gamma_+(t)} \frac{\overline{z - \zeta_+(\Gamma, t)}}{|z - \zeta_+(\Gamma, t)|^2 + \delta^2} d\Gamma \quad (29)$$

do not. Indeed, as their kernels are smooth, the resulting contribution of (29) is smooth as well. Hence, unless the Kutta condition (27) is used, the total fluid velocity has a logarithmic singularity at the plate edges.

In general however, when computing the singular integral with a quadrature rule with weights w_j ,

$$\frac{1}{2\pi i} \int_{-1}^1 \frac{\gamma_b(s, t)}{z - s} ds \approx \sum_j w_j \frac{\gamma_j}{z - s_j}$$

one introduces first-order (simple pole) singularities as z approaches the grid points s_j of the body. These first-order singularities are much stronger than the logarithmic singularities at the edges of the body. Hence these logarithmic singularities can be, and are often ignored. In section 3.3.1 we will propose a quadrature method that does not introduce any first-order singularities. In section 3.3.2 we will describe how we also remove the logarithmic singularities. These two methods help stabilize the flow near the edges and allow for more robust and accurate computation of leading-edge shedding in the simulation.

3 Numerical method

Name of equation	Equation	Discretization methods
Force balance equation	$R_1 \partial_{tt} \zeta_G(t) = -\frac{1}{2} \int_{-1}^1 [p]_+^+(s) \hat{\mathbf{n}}(s) ds - i \quad (30)$	Second-order backwards differentiation, trapezoidal rule
Torque-balance equation	$I_G \partial_{tt} \beta(t) = \int_{-1}^1 \Re \left(i \zeta_0(s) e^{i\beta(t)} (\overline{[p]_+^+(s) \hat{\mathbf{n}}(s)}) \right) ds \quad (31)$	Second-order backwards differentiation, trapezoidal rule
No-penetration condition & Kelvin's circulation theorem	$\Re \left(\overline{\hat{\mathbf{n}}(s, t)} \partial_t \zeta(s, t) \right) =$ $\Re \left(\overline{\hat{\mathbf{n}}(s, t)} \left(\frac{1}{2\pi i} \int_{-1}^1 \frac{\gamma_b(s', t)}{\zeta(s, t) - \zeta(s', t)} ds' \right. \right.$ $+ \frac{1}{2\pi i} \int_0^{\Gamma_-(t)} \frac{\overline{\zeta(s, t) - \zeta_-(\Gamma, t)}}{ \zeta(s, t) - \zeta_-(\Gamma, t) ^2 + \delta^2} d\Gamma$ $\left. \left. + \frac{1}{2\pi i} \int_0^{\Gamma_+(t)} \frac{\overline{\zeta(s, t) - \zeta_+(\Gamma, t)}}{ \zeta(s, t) - \zeta_+(\Gamma, t) ^2 + \delta^2} d\Gamma \right) \right), \quad (32)$ $\Gamma_+(t) + \Gamma_-(t) + \Gamma_b(t) = 0 \quad (33)$	See section 3.1
Suction Kutta condition	$\sigma(1, t) = \sigma(-1, t) = 0 \quad (34)$	See section 3.2
Pressure-jump equation	$[p]_+^+(s, t) = \partial_t (\Gamma_-(t) + \Gamma_b(s, t))$ $+ (\mu(s, t) - \tau(s, t)) \gamma_b(s, t), \quad (35)$ $\mu(s, t) = \Re \left(\overline{\hat{\mathbf{s}}(s, t)} \left(\frac{1}{2\pi i} \int_{-1}^1 \frac{\gamma_b(s', t)}{\zeta(s, t) - \zeta(s', t)} ds' \right. \right.$ $+ \frac{1}{2\pi i} \int_0^{\Gamma_-(t)} \frac{\overline{\zeta(s, t) - \zeta_-(\Gamma, t)}}{ \zeta(s, t) - \zeta_-(\Gamma, t) ^2 + \delta^2} d\Gamma$ $\left. \left. + \frac{1}{2\pi i} \int_0^{\Gamma_+(t)} \frac{\overline{\zeta(s, t) - \zeta_+(\Gamma, t)}}{ \zeta(s, t) - \zeta_+(\Gamma, t) ^2 + \delta^2} d\Gamma \right) \right) \quad (36)$	See section 3.3
Birkhoff-Rott equations	$\partial_t \bar{\zeta}_\pm(\Gamma, t) = \frac{1}{2\pi i} \int_{-1}^1 \frac{\gamma_b(s, t)}{\zeta_\pm(\Gamma, t) - \zeta(s, t)} ds$ $+ \frac{1}{2\pi i} \int_0^{\Gamma_-(t)} \frac{\overline{\zeta_\pm(\Gamma, t) - \zeta_-(\Gamma', t)}}{ \zeta_\pm(\Gamma, t) - \zeta_-(\Gamma', t) ^2 + \delta^2} d\Gamma'$ $+ \frac{1}{2\pi i} \int_0^{\Gamma_+(t)} \frac{\overline{\zeta_\pm(\Gamma, t) - \zeta_+(\Gamma', t)}}{ \zeta_\pm(\Gamma, t) - \zeta_+(\Gamma', t) ^2 + \delta^2} d\Gamma' \quad (37)$	See section 3.3

Name of Variable	Unknown Variable
Center-of-mass position	$\zeta_G(t)$
Angle of rotation	$\beta(t)$
Bound vortex sheet strength	$\gamma(s, t)$
Circulation of \pm sheet	$\Gamma_\pm(t)$
Pressure jump	$[p]_+^+(s, t)$
Position of the \pm sheet	$\zeta_\pm(\Gamma, t)$

These 6 equations form a closed system that allows us to determine the 6 unknown functions which completely

determine the state of the system. The main innovations in the algorithm presented lie in the treatment of the Birkhoff-Rott equations, and to a smaller extent, the pressure equation. A complete discussion of the modifications made to these equations as well as their discretizations can be found in section 3.3. A detailed outline of the steps of the algorithm can be found in section 3.4. The algorithm can be loosely described as follows. It is an implicit-explicit method that treats the body variables (body position, bound vortex sheet strength, etc.) implicitly, and the free vortex sheets explicitly. The body is initialized at rest with zero pressure jump and vortex sheet strength. At each time step we perform the following procedure. The free sheets are evolved explicitly forward by one time step dt using the Birkhoff-Rott equations (37). The body is then evolved implicitly forward by dt using the force- (30) and torque-balance (31) equations. Simultaneously, a new mesh point on the \pm free sheet is placed on the corresponding \pm edge that connects to it. This mesh point has circulation determined by the suction Kutta condition (34). In solving for the forces that dictate the body's motion, the pressure-jump equation (35) is solved for the pressure, and the no-penetration condition (32) is solved for the bound vortex sheet strength. All these quantities are solved for implicitly along with the body's new position using Broyden's method. The procedure is then repeated.

3.1 No-penetration condition & Kelvin's circulation theorem

We handle the time derivatives with second-order backward differentiation. The body's arc-length parameter s is discretized with two interlaced grids, the Chebyshev nodes of the first and second kinds respectively:

$$s_j^{1\text{st}} = -\cos(\pi(2j+1)/(2n)), \quad j = 0, \dots, n-1; \quad s_j^{2\text{nd}} = -\cos(\pi j/n), \quad j = 0, \dots, n.$$

We seek to compute the bound vortex sheet strength $\gamma_b(s, t)$ at the $\{s_j^{2\text{nd}}\}$ by enforcing the no-penetration condition at the $\{s_j^{1\text{st}}\}$, similar to the collocation method for the airfoil equation in [Gol90]. Hence, we discretize the singular integral in (32) as

$$\frac{1}{2\pi i} \int_{-1}^1 \frac{\gamma_b(s', t)}{\zeta_j^{1\text{st}} - \zeta(s', t)} ds' \approx \sum_{k=0}^n w_k \frac{\gamma_j^{2\text{nd}}}{\zeta_j^{1\text{st}} - \zeta_k^{2\text{nd}}} \quad (38)$$

and discretize Kelvin's circulation theorem (33) using

$$\Gamma_b(t) = \int_{-1}^1 \gamma_b(s, t) ds \approx \sum_{k=0}^n w_k \gamma_j^{2\text{nd}}. \quad (39)$$

Here, w_k are the weights of the trapezoidal rule on the grid points of the second kind. The remaining integrals in (32) need special treatment. Their discretization is discussed in section 3.3.1 alongside the similar terms in the Birkhoff-Rott equation (37). By substituting (38) into (32), and (39) into (33) we obtain a linear system of $n+1$ equations in the $n+1$ unknowns $\gamma_j^{2\text{nd}}$. Solving these yields the $n+1$ values $\gamma_j^{2\text{nd}}$.

3.2 Kutta condition

To discretize (34) we need to obtain a discretization of the suction function $\sigma(s, t)$, which we denote $\sigma_j^{2\text{nd}}$. The discretized Kutta condition can then be written as

$$\begin{aligned} \sigma_0^{2\text{nd}} &= 0, \\ \sigma_n^{2\text{nd}} &= 0 \end{aligned} \quad (40)$$

If we were to apply the formula $\sigma(s, t) = \sqrt{1-s^2}\gamma(s, t)$ to discretize σ , then we would have $\sigma_j^{2\text{nd}} = \sqrt{1-(s_j^{2\text{nd}})^2}\gamma_j^{2\text{nd}}$. Regardless of the values of $\gamma_j^{2\text{nd}}$, this would force $\sigma_j^{2\text{nd}} = \sqrt{1-1}\gamma_j^{2\text{nd}} = 0$ for $j = 0, n$. Equation (40) will then hold trivially, making it redundant. σ is thus discretized as follows. First, we use Chebyshev interpolation to interpolate γ from the points of the second kind to the first kind, hence obtaining the n values $\gamma_j^{1\text{st}}$. We may thus form $\sigma_j^{1\text{st}} = \gamma_j^{1\text{st}} \sqrt{1-s_j^{1\text{st}}}$. Now, we may interpolate back to the points of the second kind using Chebyshev interpolation again to obtain the $n+1$ points $\sigma_j^{2\text{nd}}$. Henceforth we suppress the superscript "2nd" for readability so that $s_j = s_j^{2\text{nd}}$, $\zeta_j = \zeta_j^{2\text{nd}}$, and $\gamma_j = \gamma_j^{2\text{nd}}$.

3.3 Birkhoff-Rott and pressure-jump equations

We now discuss the the numerical treatment of both the Birkhoff-Rott equations and the pressure-jump equation. Third-order Adams-Bashforth is used to evolve the former, while second-order backward differentiation is used for the latter. The principal issue we address is the discretization of the Cauchy integral

$$\frac{1}{2\pi i} \int_{-1}^1 \frac{\gamma_b(s', t)}{z - \zeta(s', t)} ds' \quad (41)$$

with $z = \zeta(s, t)$ or $\zeta_{\pm}(\Gamma, t)$. We begin by developing a simple quadrature rule to compute such integrals.

3.3.1 Log quadrature

Recall the Birkhoff-Rott equations (37) for the velocity of the free sheets. In computing the velocity induced by the body, one evaluates the Cauchy integral (41) with z on the free sheet. Should z lie on the body as well, this Cauchy integral is of principal-value type, and there are simple quadrature methods that compute the

integral accurately [Boi01]. When z is far from the body, the integrand is smooth, and standard quadrature methods such as the trapezoidal rule yield accurate results. However, in simulating the long-time behavior of a falling body, the free vortex sheets often lie very close to the body but not on it. In this near-singular integral situation, the standard quadrature methods are inaccurate, and the quadrature methods for principal valued integrals do not apply. A new approach is needed. Recently, Nitsche proposed to evaluate 1D near-singular integrals based on the addition of error-correcting terms [Nit21]. It was employed in [Soh24] to compute the vortex wake of a falling plate. Here, we propose an alternative method to handle these near-singular integrals that achieves similar results, but in the opinion of the authors, is easier to implement. This method can be applied to flexible bodies as well.

As noted in section 2.4, discretizing this singular integral using the trapezoidal rule:

$$\frac{1}{2\pi i} \int_{-1}^1 \frac{\gamma_b(s, t)}{z - \zeta(s, t)} \approx \sum_j w_j \frac{\gamma_j}{z - \zeta_j},$$

introduces first-order singularities on each of the grid points of the body. Here w_j are the quadrature weights. While the computed velocity at z blows up as it approaches the body, the true velocity remains bounded. Near the body, this mismatch between the computed and true velocities gives rise to significant errors. The principle behind the trapezoidal rule is that the integrand can be approximated by a piecewise linear function, which can then be integrated exactly. In the method described below, instead of approximating the singular integrand as a piecewise-linear function, we approximate a smooth term inside the integrand as a piecewise-linear function, and then compute the integral analytically, thereby obtaining an accurate approximation.

To begin, recall that we discretize the body's arc-length parameter s using a Chebyshev grid points of the second kind with $n + 1$ points. Let them be $s_j = s_j^{\text{2nd}} = -\cos(\frac{j\pi}{n})$, $j = 0, 1, 2, \dots, n$. Let $\Gamma_j = \Gamma_b(s_j, t)$ and $\zeta_j^{\text{2nd}} = \zeta_j = \zeta(s_j, t)$, and recall that the circulation on the body is given by $\Gamma_b(s, t)$ where

$$\Gamma_b(s, t) = \int_{-1}^s \gamma_b(s', t) ds'.$$

Then, we may write

$$\begin{aligned} \int_{-1}^1 \frac{\gamma_b(s, t)}{z - \zeta(s, t)} ds &= \int_{\Gamma_0}^{\Gamma_n} \frac{d\Gamma}{z - \zeta(\Gamma, t)} \\ &= \sum_{j=0}^{n-1} \int_{\Gamma_j}^{\Gamma_{j+1}} \frac{d\Gamma}{z - \zeta(\Gamma, t)}. \end{aligned}$$

Now, by analogy with the trapezoidal rule, we make the assumption that $\zeta(\Gamma, t)$ is a linear function of Γ on each subinterval $[\Gamma_j, \Gamma_{j+1}]$ and integrate exactly. On each subinterval $[\Gamma_j, \Gamma_{j+1}]$, we have

$$\zeta(\Gamma, t) = a_j \Gamma + b_j$$

where

$$a_j = \frac{\zeta_{j+1} - \zeta_j}{\Gamma_{j+1} - \Gamma_j}$$

and

$$b_j = \frac{\zeta_j \Gamma_{j+1} - \zeta_{j+1} \Gamma_j}{\Gamma_{j+1} - \Gamma_j}.$$

It immediately follows that

$$\begin{aligned} \int_{\Gamma_j}^{\Gamma_{j+1}} \frac{d\Gamma}{z - \zeta(\Gamma, t)} &\approx -\frac{1}{a_j} \int_{\Gamma_j}^{\Gamma_{j+1}} \frac{d\Gamma}{\Gamma - \frac{z - b_j}{a_j}} \\ &= -\frac{1}{a_j} (\log(a_j \Gamma_{j+1} + b_j - z) - \log(a_j \Gamma_j + b_j - z)) \\ &= -\frac{1}{a_j} (\log(\zeta_{j+1} - z) - \log(\zeta_j - z)) \end{aligned}$$

Therefore,

$$\frac{1}{2\pi i} \int_{-1}^1 \frac{\gamma_b(s, t)}{z - \zeta(s, t)} ds \approx \frac{-1}{2\pi i} \sum_{j=0}^n \frac{1}{a_j} (\log(\zeta_{j+1} - z) - \log(\zeta_j - z)) \quad (42)$$

In summary, to compute near-singular integrals without sampling the integrand, we first subdivide the body into smaller subintervals. On each subinterval, we assume the body position ζ is a piecewise linear function of circulation, and evaluate the integral exactly. Then, we sum the contributions of each segment to obtain the total contribution of the body to the flow. By doing so, we weaken the singularities in the computed flow from $O(\frac{1}{z - \zeta_j})$ to $O(\log(z - \zeta_j))$, which allows for a more accurate computation of the velocity of the free vortex sheets. A similar method was used to compute frictional forces accurately in [Alb13]. Similar formulae can be obtained even in the presence of blob regularization. Indeed, for consistency, we evaluate the contributions of the free sheets to the fluid velocity using a similar formula

$$\begin{aligned} \frac{1}{2\pi i} \int_0^{\Gamma_{\pm}(t)} \frac{\overline{z - \zeta_{\pm}(\Gamma', t)}}{|z - \zeta_{\pm}(\Gamma', t)|^2 + \delta^2} d\Gamma' &\approx \sum_{j=0}^{k_{\pm}} \frac{-1}{a_j 2\pi i} \left(\frac{1}{2} \log \left(\frac{(\Gamma_{\pm,j+1} - c_j^R)^2 + (c_j^I)^2 + \delta^2}{(\Gamma_{\pm,j} - c_j^R)^2 + (c_j^I)^2 + \delta^2} \right) \right. \\ &\quad \left. + \frac{ic_j^I}{(c_j^I)^2 + \delta^2} \left(\arctan \left(\frac{\Gamma_{\pm,j+1} - c_j^R}{\sqrt{(c_j^I)^2 + \delta^2}} \right) - \arctan \left(\frac{\Gamma_{\pm,j} - c_j^R}{\sqrt{(c_j^I)^2 + \delta^2}} \right) \right) \right). \end{aligned} \quad (43)$$

Here, $c_j = \frac{z - b_j}{a_j}$, and a_j, b_j are given as before. $c_j^R = \Re c_j$ and $c_j^I = \Im c_j$ so that $c_j = c_j^R + ic_j^I$. See appendix B for more details. Note that the formula (42) is the limit of (43) (but for the bound instead of free vortex sheets) as $\delta \rightarrow 0$.

The method described thus far can be interpreted in the following way. It treats the plate as a *hybrid* between a 0-dimensional and a 1-dimensional vortex structure. Indeed, when using equation (38), one implicitly solves for γ_b by treating the plate as a collection of $n+1$ 0-dimensional point vortices with circulation $w_j \gamma_j^{2\text{nd}}$, $j = 0, 1, \dots, n$. Later however, when using γ_b to compute the velocity induced by the bound vortex sheet, it is treated instead as a 1-dimensional vortex structure to reduce the $1/(z - \zeta_j)$ singularities to $\log(z - \zeta_j)$ singularities via integration.

3.3.2 Velocity-smoothing the pressure-jump and Birkhoff-Rott equations

As discussed in both section 2.4, and appendix A, the Cauchy integral

$$\frac{1}{2\pi i} \int_{-1}^1 \frac{\gamma_b(s, t)}{z - \zeta(s, t)} ds \quad (44)$$

can introduce logarithmic singularities into the flow at the edges of the body. These logarithmic singularities are analogous to the logarithmic singularities on the grid points of the body introduced by the log quadrature rule (42). Methods have been developed to eliminate these logarithmic singularities that appear on the body's edges without forcing γ to vanish at the edges. Two such methods appear in [Alb10b], “tapered smoothing” and “velocity smoothing.” In the tapered-smoothing method, δ is no longer uniform, but rather a function of the arc length parameter of the vortex sheet, $\delta(s)$. As $s \rightarrow \pm 1$, the edges of the body, δ tapers to 0, thereby removing the logarithmic singularities on the body's edges. Tapered smoothing has been applied successfully in several studies such as [Soh24] and [Alb+12].

For falling bodies however, the dynamics of the system is dominated by leading-edge effects. The computed dynamics are thus sensitive to the motions of the vortex sheets near the leading edge. As observed in [Alb10b], accurately computing the motions of the sheets regularized by δ requires the local mesh spacing on the vortex sheets to be proportional to δ . Indeed, this is a general feature of vortex blob methods, which require the vortex cores to overlap in order for convergence properties to hold [KL93]. Since our equations are nondimensionalized by the terminal velocity of the body, the speed of the body is $O(1)$. Hence as the points on the vortex sheet are released from the body edges at each time step and advect with the local flow speed, the mesh spacing near the body edges needs to be proportional to $dt \cdot O(1) = O(dt)$ for accurate evolution of the sheets near the body edges. In the tapered-smoothing method, since δ tapers to 0 near the edge, it becomes difficult to evolve the sheets near the edges accurately without a priori knowledge of the initial shape of the vortex sheet leaving the edge. (See [Alb10b] for one such example.) Therefore, a method that accurately computes the flow of the free sheets near the edge while simultaneously suppressing the logarithmic singularities there is desirable.

Here we propose a lightly modified version of the method of velocity smoothing that allows for exactly that. It can be described as follows. When computing the velocities of the free sheets close to the body in (37), the Cauchy integral representing the contribution of the bound vortex sheet to the fluid velocity is smoothed as well. That is, for points sufficiently close to the body, the integral

$$\frac{1}{2\pi i} \int_{-1}^1 \frac{\gamma_b(s, t)}{\zeta_{\pm}(\Gamma, t) - \zeta(s, t)} ds \quad (45)$$

is replaced with

$$\frac{1}{2\pi i} \int_{-1}^1 \frac{\overline{\zeta_{\pm}(\Gamma, t) - \zeta(s, t)}}{|\zeta_{\pm}(\Gamma, t) - \zeta(s, t)|^2 + \delta^2} \gamma_b(s, t) ds \quad (46)$$

for such points, with δ uniform on the free sheets. Near the body, one favors (46) which suppresses the logarithmic singularities nearby. On the other hand, further from the body, the singularities are weak enough that one instead favors (45) which occurs in the exact no-penetration condition. Let $l(\zeta)$ denote the distance from ζ to the body. Then consider a C^{∞} smooth transition function

$$B(l) = \begin{cases} 0, & \text{if } l = 0, \\ \frac{\exp(-\delta/l)}{\exp(-\delta/l) + \exp(-\delta/(1-l))}, & \text{if } 0 < l < 1, \\ 1, & \text{if } l \geq 1. \end{cases}$$

The contribution of the body to the velocity of the free sheets is given by

$$\frac{B(l(\zeta))}{2\pi i} \int_{-1}^1 \frac{\gamma_b(s, t)}{\zeta_{\pm}(\Gamma, t) - \zeta(s, t)} ds + \frac{1 - B(l(\zeta))}{2\pi i} \int_{-1}^1 \frac{\overline{\zeta_{\pm}(\Gamma, t) - \zeta(s, t)}}{|\zeta_{\pm}(\Gamma, t) - \zeta(s, t)|^2 + \delta^2} \gamma_b(s, t) ds. \quad (47)$$

The blending function B was chosen since it smoothly transitions from 0 to 1 over a distance δ . Moreover,

$$\frac{d^m}{dl^m} B(l) = 0 \text{ for every integer } m \geq 0 \text{ and } l = 0, \delta.$$

That is to say, the function B approaches 0 and 1 with infinite order at $l = 0$ and $l = \delta$ respectively. Hence, as ζ_{\pm} approaches the edge, the velocity induced by the body on ζ_{\pm} blends from singular to smoothed with infinite order over a distance δ . As observed in [Alb10b], this procedure improves the smoothing error from $O(\delta^{1/2})$ to $O(\delta^{3/2})$ in simple model problems.

Thus, in this study, we evolve the sheets with the velocity-smoothed Birkhoff-Rott equations given by

$$\begin{aligned} \partial_t \bar{\zeta}_{\pm}(\Gamma, t) = & \frac{B(l(\zeta_{\pm}))}{2\pi i} \int_{-1}^1 \frac{\gamma_b(s, t)}{\zeta_{\pm}(\Gamma, t) - \zeta(s, t)} ds + \frac{1 - B(l(\zeta_{\pm}))}{2\pi i} \int_{-1}^1 \frac{\overline{\zeta_{\pm}(\Gamma, t) - \zeta(s, t)}}{|\zeta_{\pm}(\Gamma, t) - \zeta(s, t)|^2 + \delta^2} \gamma_b(s, t) ds \\ & + \frac{1}{2\pi i} \int_0^{\Gamma_{-}(t)} \frac{\overline{\zeta_{\pm}(\Gamma, t) - \zeta_{-}(\Gamma', t)}}{|\zeta_{\pm}(\Gamma, t) - \zeta_{-}(\Gamma', t)|^2 + \delta^2} d\Gamma' + \frac{1}{2\pi i} \int_0^{\Gamma_{+}(t)} \frac{\overline{\zeta_{\pm}(\Gamma, t) - \zeta_{+}(\Gamma', t)}}{|\zeta_{\pm}(\Gamma, t) - \zeta_{+}(\Gamma', t)|^2 + \delta^2} d\Gamma'. \end{aligned} \quad (48)$$

instead of (37). We handle the pressure-jump equation in a similar way. That is, when computing $\mu(s, t)$ in the pressure-jump equation (35), we smooth plate's contribution to the fluid velocity $\mu(s, t)$ as well. Hence we use the following equation for $\mu(s, t)$ instead of (36):

$$\begin{aligned} \mu(s, t) = \Re \left(\overline{\hat{s}(s, t)} \left(\frac{1}{2\pi i} \int_{-1}^1 \frac{\overline{\zeta_{\pm}(\Gamma, t) - \zeta(s, t)}}{|\zeta_{\pm}(\Gamma, t) - \zeta(s, t)|^2 + \delta^2} \gamma_b(s, t) ds + \frac{1}{2\pi i} \int_0^{\Gamma_{-}(t)} \frac{\overline{\zeta(s, t) - \zeta_{-}(\Gamma, t)}}{|\zeta(s, t) - \zeta_{-}(\Gamma, t)|^2 + \delta^2} d\Gamma \right. \right. \\ \left. \left. + \frac{1}{2\pi i} \int_0^{\Gamma_{+}(t)} \frac{\overline{\zeta(s, t) - \zeta_{+}(\Gamma, t)}}{|\zeta(s, t) - \zeta_{+}(\Gamma, t)|^2 + \delta^2} d\Gamma \right) \right). \end{aligned} \quad (49)$$

In equations (48) and (49), the smoothed Cauchy integrals are discretized using the log-quadrature rule discussed in the preceding section, 3.3.1.

3.3.3 Controlling the no-penetration error with sub-step fencing

Following [Alb09], each time step consists of two sub-steps. During the first sub-step, the free sheets are evolved (explicitly) using the Birkhoff-Rott equation (37) and the log-quadrature rule discussed in section 3.3.1. In the second sub-step, the body is evolved (implicitly) using both the force-balance (30) and torque-balance (31) equations. During this sub-step, the vortex strength γ_b and pressure jump $[p]_{-}^{+}$ are determined using the no-penetration equation (32) and pressure-jump equation (35) respectively. As discussed in section 3.1, during the implicit sub-step where the body moves, the no-penetration equation (32) is used to obtain γ_b as a function of the quantities $\zeta(s, t)$, $\partial_t \zeta(s, t)$, $\zeta_{\pm}(\Gamma, t)$ and $\Gamma(s, t)$ by inverting a Cauchy integral.

This approach is insufficient to enforce the no-penetration condition strictly because the free vortex sheets and body may interpenetrate during both the implicit and explicit sub-steps. During the implicit sub-step, the free sheets are fixed, and the body moves through the fluid. Although the no-penetration condition is used to determine the bound vortex sheet strength γ_b , the plate may pass through the free vortex sheet on this sub-step due to temporal and spatial discretization errors. During the explicit sub-step, the free sheets may pass through the body for the same reason. An additional source of error on the explicit sub-step is the use of velocity smoothing, which introduces additional error into the no-penetration condition. Indeed, since γ_b is obtained with zero smoothing on the plate, by advecting the vortex sheets with smoothing on the plate in the Birkhoff Rott equations (48), one introduces an error of size $O(\delta)$ into the no-penetration condition near the body as the price for removing logarithmic singularities in the flow. Note that there is an analogous source of error during the implicit sub-step incurred by blob regularizing the free sheets.

Interpenetration of the body and free sheets can be controlled by the following procedure termed “sub-step fencing.” After the body moves in the implicit sub-step, or the sheets move in the explicit sub-step, we identify all points on the free vortex sheets that pass through the plate. We decompose their displacements into components normal and tangential to the body. We set the normal component to be the distance to the body minus a small value (10^{-6}). A crucial detail is that this sub-step fencing procedure needs to be applied during each iteration of nonlinear solver used to solve the discretized system of equations in the implicit sub-step. In effect, the velocity of each crossing point is projected tangentially along the body, ensuring that streamlines do not pass through the body, which obeys the no-penetration condition.

Another approach to fencing, used by [Pan+12], is to project the points only once at the end of each full time step, and place them a fixed distance away from the body. We find that the more-frequent fencing that we use—during each sub-step, including within the iterative solver—is necessary because if any point on the free sheet passes through the body at some sub-step, the discontinuity of the fluid velocity across the body introduces a large error in the velocities computed at the next sub-step. Furthermore, as the free sheets are evolved using the multi-step method third-order Adams-Bashforth, third-order accuracy is only possible if the velocity field varies smoothly over the trajectory of the point. For a point that passes through the body however, this condition is violated, and we lose third-order accuracy.

3.4 Outline of the coupled fluid-body solver

We now outline the major steps of the algorithm, focusing on the novel aspects. A convergence can be found for select cases in appendix C.

Algorithm 1 Coupled fluid-body solver for a falling rigid body

for each time step $k = 1, 2, \dots$ do

Step 1: Evolve vortex sheets explicitly to obtain $\zeta_{\pm}(\Gamma, t)$:

- Use the velocity-smoothed Birkhoff-Rott equations (48) (section 3.3.2).
- Use the log-desingularized quadrature rules (42), (43) to discretize the integrals (section 3.3.1).

Step 2: Sub-step fence:

- Project all crossing vortex points normally to the body surface to prevent crossing. (section 3.3.3).

Step 3: Compute the 5 (real) unknown body variables at the current time step implicitly by solving the following nonlinear system of 5 (real) discretized equations iteratively:

Equations for the nonlinear solver:

- Force balance equation (30) (2 real equations)
- Torque balance equation (31)
- Kutta condition on each edge (34) (2 real equations)

Unknown variables for the nonlinear solver:

- Center-of-mass position $\zeta_G(t)$ (2 real variables)
- Angle of rotation from initial rest state $\beta(t)$
- Total circulation of sheets $\Gamma_{\pm}(t)$ (2 real variables)

At each iteration of the nonlinear solver:

- Sub-step fence again, and project all crossing vortex points onto plate as it moves (section 3.3.3).
- Use the collocation method to obtain $\gamma_b(s, t)$ (section 3.1).
- Use the pressure-jump equations (35) to compute the pressure jump $[p]_+^+$ from $\gamma_b(s, t)$.
- Interpolate $\gamma_b(s, t)$ to obtain $\sigma(\pm 1, t)$ for use in the Kutta condition (section 3.2).

end for

4 Dynamics of falling plates

Here, we report results on the dynamics of flat plates and a family of curved plates obtained by bending the flat plate symmetrically about its center. The flat plate is a special case that, unlike the curved plates, can move purely tangentially by translating in the in-plane direction. In the inviscid model without viscous skin friction, such a motion can result in very small or even zero vortex sheet strengths and pressure forces on the plate, and thus unrealistically large plate velocities under gravitational forces. To obtain realistic dynamics for the flat plate, we add an additional term to the right-hand side of the force balance equation (30) to account for skin friction as was done in [Alb+12].

4.1 The flat plate

4.1.1 Including skin friction

We assume that the skin friction at a given point on the flat plate can be approximated by that of the Blasius boundary layer on a flat plate in a steady oncoming flow. The velocity in the Blasius skin friction formula is set to V_{avg} , the (tangential) difference between the plate and flow velocity, averaged along the plate and over both sides. This model is similar to that in [Alb+12] (which approximated V_{avg} by the negative plate velocity). The traction is thus equal to that which would be induced by a Blasius boundary layer attached to the flat plate. For the moment, let us use dimensional variables. Following the assumption, the surface traction induced by skin friction is approximately [Bat67]

$$\tau_{skin} = \frac{1}{3} \exp(i\beta) \rho_f \hat{V}_{avg} \sqrt{\nu \frac{|V_{avg}|^3}{L + \hat{V}_{avg} s}}. \quad (50)$$

Here, ν is the kinematic viscosity, $\hat{V}_{avg} = \frac{V_{avg}}{|V_{avg}|}$, and β is the angle of the plate (relative to the horizontal axis). As the body has 2 sides, total viscous drag is given by

$$F_{visc} = 2 \exp(i\beta) \int_{-L}^L \frac{1}{3} \rho_f \hat{V}_{avg} \sqrt{\nu \frac{|V_{avg}|^3}{L + \hat{V}_{avg} s}} ds = \frac{4\sqrt{2L\nu}}{3} \exp(i\beta) \rho_f |V_{avg}|^{\frac{3}{2}} \hat{V}_{avg}. \quad (51)$$

We add this term to the right-hand side of (3) to obtain

$$\rho_b h W 2L \partial_{tt} \zeta_G(s) = W \int_{-L}^L [p]_+^+(s) \hat{\mathbf{n}}(s) ds - i \rho_b h W 2L g + \frac{4\sqrt{2L\nu}}{3} \exp(i\beta) \rho_f |V_{avg}|^{\frac{3}{2}} \hat{V}_{avg}. \quad (52)$$

Nondimensionalising as before,

$$R_1 \partial_{tt} \zeta_G(s) = -\frac{1}{2} \int_{-1}^1 [p]_+^+(s) \hat{\mathbf{n}}(s) ds - i + \frac{2\sqrt{2}}{3\sqrt{Re}} \exp(i\beta) |V_{avg}|^{\frac{3}{2}} \hat{V}_{avg}. \quad (53)$$

Here, $Re = \frac{UL}{\nu}$ is the Reynolds number, which we fix as $Re = 10^3$ for the remainder of this study. As shown above, the drag induced by skin friction is $O(1/\sqrt{Re})$. Following the analysis in [HJR66], the necessary modification to (53) to account for a body with small curvature involves the inclusion of additional terms of order $O(1/Re)$. Hence, in the inviscid limit, (53) can be thought of as a low-order model for plates that are flat or slightly curved. Here we use skin friction for flat plates only.

4.1.2 Physical and numerical parameter values

The plates are released from rest at a fixed initial angle. Each free vortex sheet ζ_{\pm} is initialized as a single line segment with two endpoints, located at distances of 10^{-5} and 2×10^{-5} away from the \pm edges, respectively, in the direction tangent to the plate. Both free vortex sheets have zero initial circulations. We discretize the body's arc-length parameter s using a Chebyshev grid with $n = 100$ points (section 3.1), and use a time step $dt = 0.012$. More details can be found in appendix C. In table 2 we show the exact values of R_1 and initial angles used to obtain the results in the subsequent subsections. In table 3 we describe the steady-state dynamical motions observed in different R_1 ranges. Each of the dynamical motions—“fluttering,” “mixed,” “tumbling,” “looping,” and “autorotating”—are described and defined as they arise in the subsequent subsections.

Initial angles	$0^\circ, 4.5^\circ, 9^\circ, 13.5^\circ, \dots, 45^\circ$
R_1	$0, 0.01, \dots, 0.1, 0.2, \dots, 5, 10, 100, 500, 1000$

Table 2: Values of the physical parameters used for the falling flat plates

R_1	$[0, 0.2)$	$[0.2, 0.6)$	$[0.6, 1.5)$	$[1.5, 2.6)$	$[2.6, 1000)$
Steady-state dynamics	Fluttering	Mixed	Tumbling	Looping	Autorotating

Table 3: Ranges of R_1 and corresponding steady-state dynamics.

4.1.3 $R_1 < 0.2$: the pure fluttering regime

In this R_1 range the dominant steady-state motion is small-amplitude side-to-side fluttering as shown in figure 2. In panels (a) and (b) we show the trajectory of the center of mass and the vortex wake formed behind a plate undergoing small-amplitude fluttering at $R_1 = 0.02$. In this study, a body is said to be “fluttering” if both its angular velocity and the horizontal velocity of its center of mass change sign as it falls, corresponding to a side-to-side oscillation while falling. The speed of the center of mass often vanishes, resulting in the sharp cusps in its trajectory in figure 2(a). Panel (b) shows that the vortex wake is highly irregular, its structure disturbed by repeated collisions with the fluttering plate.

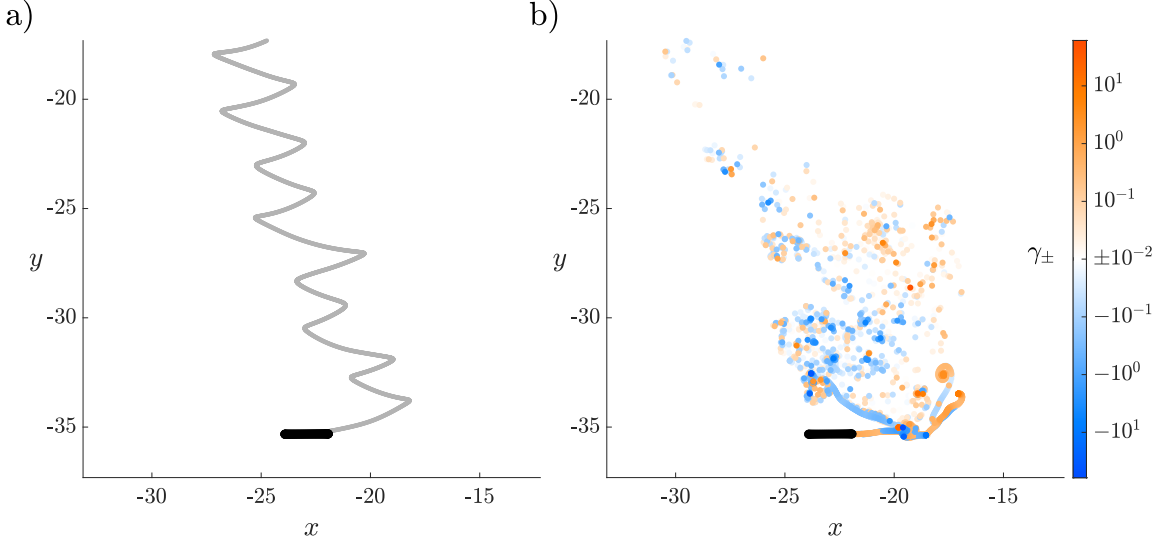


Figure 2: Side-by-side comparison between (a) the trajectory of the center of mass and (b) the chaotic vortex wake formed by a falling plate with $R_1 = 0.02$ undergoing small-amplitude fluttering.

In figure 3, in each panel labeled by R_1 , we show the trajectories of the center of mass of a falling plate for various initial angles listed in table 2. Each panel contains an inset showing a larger range. The red rectangle in the inset indicates the close-up portion of the trajectories shown in the main panel. Each panel is shaded according to the steady-state dynamics exhibited by the falling plates. As seen in the panels of figure 3 (and later in figure 9 for $R_1 < 0.7$), increasing R_1 increases the side-to-side fluttering amplitude. Occasionally, the side-to-side fluttering motion is punctuated by a much faster diving motion, shown the large arcs in figure 3 when $R_1 \geq 0.05$. These occur when the plate collides with its own vortex wake, which can sometimes destabilize it into this faster falling motion.

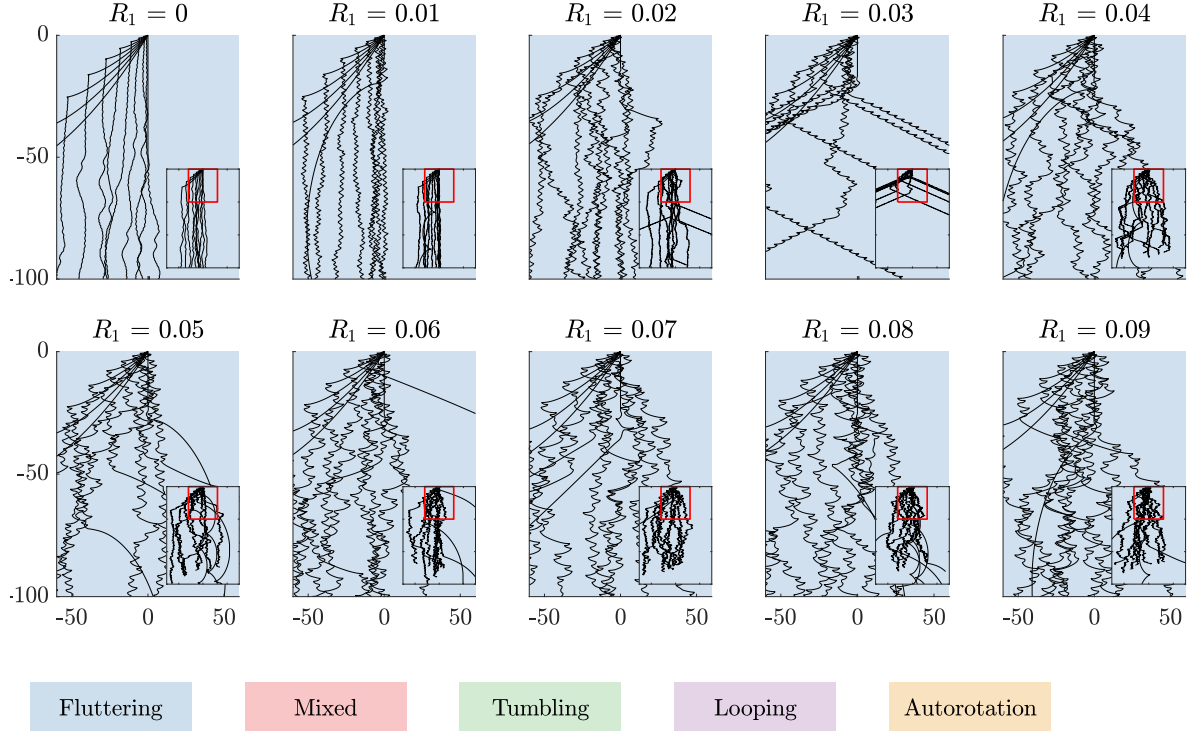


Figure 3: For $R_1 = 0, 0.01, \dots, 0.09$, snippets of the center-of-mass trajectories of falling plates for ten initial angles within $[0, \pi/4]$ during $0 \leq t \lesssim 500$. The plots are shaded according to the qualitative dynamics exhibited by the steady state. Within this R_1 range, only fluttering motions occur. Each panel contains an inset that shows the large-scale features of the same trajectories, with a red rectangle indicating the portion shown in the main panel.

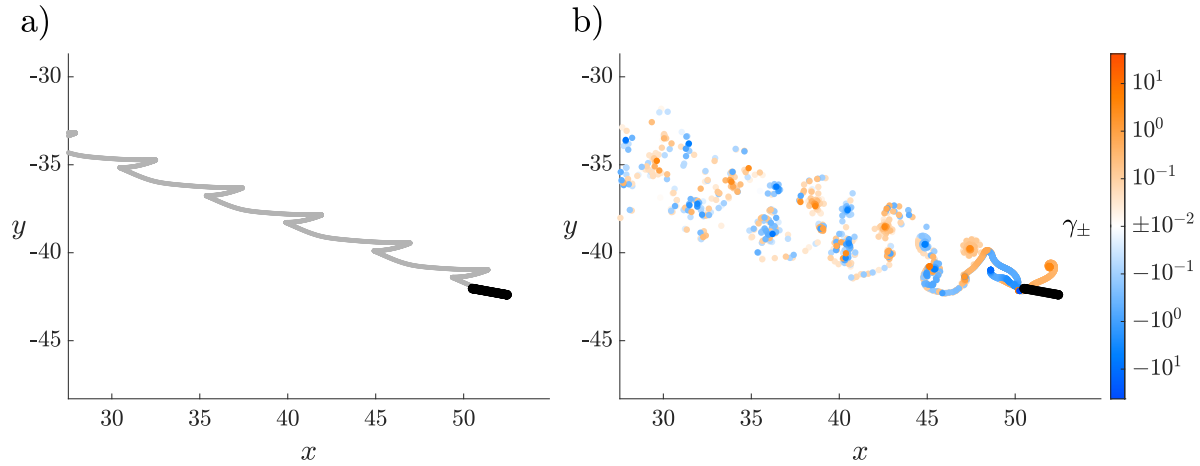


Figure 4: The trajectory of the center of mass (a) and the vortex wake (b) formed by a falling plate with $R_1 = 0.03$ undergoing progressive fluttering.

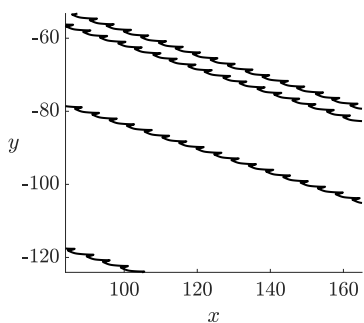


Figure 5: Plate trajectories when $R_1 = 0.03$ for initial angles $4.5^\circ, 22.5^\circ, 36^\circ, 45^\circ$. All trajectories simulated (including those not shown) converge to steady-state periodic fluttering at this value of R_1 .

As suggested by the vortex wake shown in figure 2(b), the steady-state side-to-side fluttering motions within this regime are chaotic, i.e. sensitive to both initial conditions and numerical parameters. This is shown more clearly in appendix C. These fluttering motions can change sharply with R_1 , and for some values of R_1 can switch dramatically from irregular and erratic, to periodic. For example, all trajectories are eventually periodic at $R_1 = 0.03$ but rarely at 0.02 and not at 0.04. The wake behind one such periodic trajectory is shown in figure 4, and periodic trajectories with $R_1 = 0.03$ and four initial angles are shown in figure 5.

When $R_1 = 0.03$ all falling plates oscillate about a diagonal path with a fixed nonzero angle from vertical (see figure 5). This is because the translational and rotational velocities are periodic, the latter with mean zero. Hence, the plate traverses a fixed distance in both the horizontal and vertical directions in each period. A close-up of these periodic trajectories is shown in figure 5. This staircase-like periodic fluttering motion observed here at $R_1 = 0.03$ was also found by [Li+22] and [PR24] and termed “progressive fluttering.” There, this falling mode was found at $I^* = 0.1$, or $R_1 \approx 0.23$. However, in their model, the center of equilibrium of the plate

was shifted to one side which could explain the difference. Progressive fluttering is also observed for some initial angles when $R_1 = 0.02$ as can be seen from the straight diagonal lines in the inset of figure 3 at this R_1 .

4.1.4 $0.2 \leq R_1 < 0.7$: the mixed-fluttering-and-tumbling regime

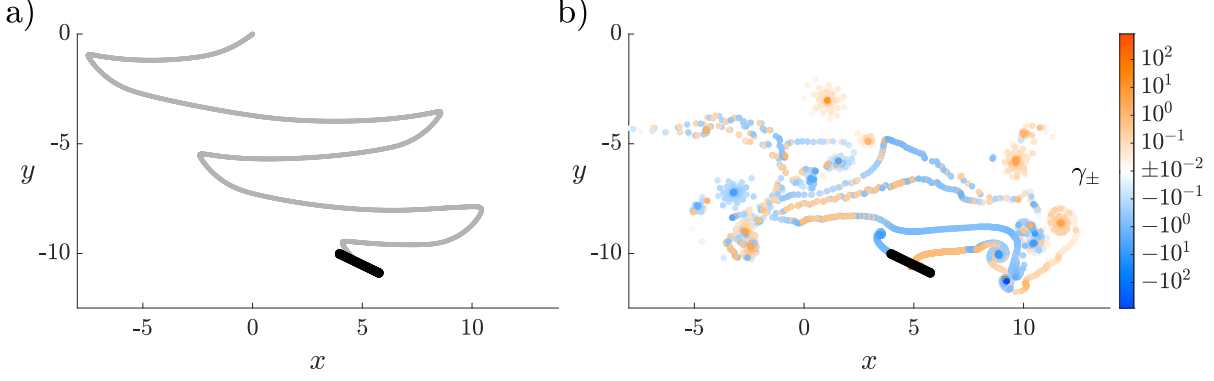


Figure 6: The trajectory of the center of mass (a) and the vortex wake (b) formed by a falling plate with $R_1 = 0.3$ undergoing large-amplitude fluttering.

As R_1 increases past 0.1, the fluttering amplitude begins to increase, resulting in a more regular vortex wake behind the fluttering plates. An example is shown in figure 6(b). Figure 7 shows a schematic diagram of this vortex wake. It consists of an array of asymmetric dipoles formed by large and small vortex cores. Figure 8 shows an example of the formation of such a dipole, at four successive times in panels (a-d).

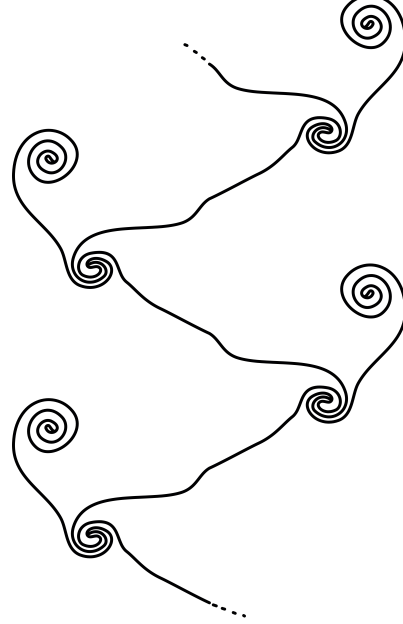


Figure 7: Schematic diagram showing the typical dipole vortex wake structure behind a plate undergoing large-amplitude fluttering. Each asymmetric dipole consists of large and small vortices. The large vortex is shed from the leading edge as it decelerates, while the smaller vortex is shed from the same edge as the plate begins to accelerate.

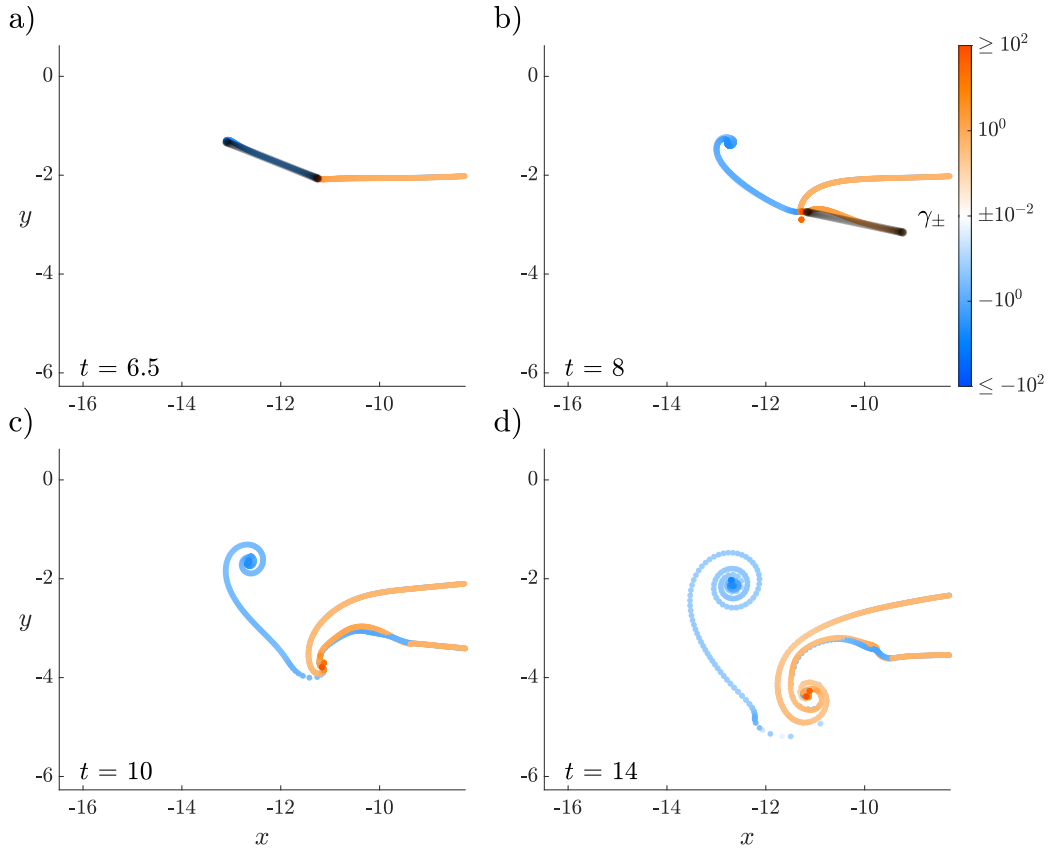


Figure 8: The formation and evolution of a dipole shed from a fluttering plate with $R_1 = 0.2$. Panels (a-d) show snapshots at times $t = 6.5, 8, 10, 14$, and the dipole that forms as the plate reverses direction, with a cusp in its trajectory.

The formation of the dipole in figure 8 can be explained intuitively as follows. When the plate stops moving leftward and starts moving rightward (panel (a)), the angular momentum of the plate rapidly changes sign *twice*. In tandem with each of these large angular impulses is a corresponding release of vorticity into the fluid. The first sign change occurs just before it reverses direction, and its leading edge (left edge) becomes its trailing edge. Corresponding to this large angular impulse, a large vortex is formed at the left edge. This negative (blue) vortex is shown in panels (a-b) of figure 8. As the plate begins to move rightward, its angular velocity changes sign again. In tandem with this second angular impulse, another vortex is released from the right (leading) edge as it moves. This is shown in panels (b-c) of figure 8. Together, these two vortices from one of the dipoles shown in the schematic shown in figure 7, and can be seen in panels (c-d) of figure 8. This transient dipole wake structure resembles the photographs of the experiments of [BEM98] and can be seen in the supplementary movie “[movie_0.35_flatplate.avi](#)”.

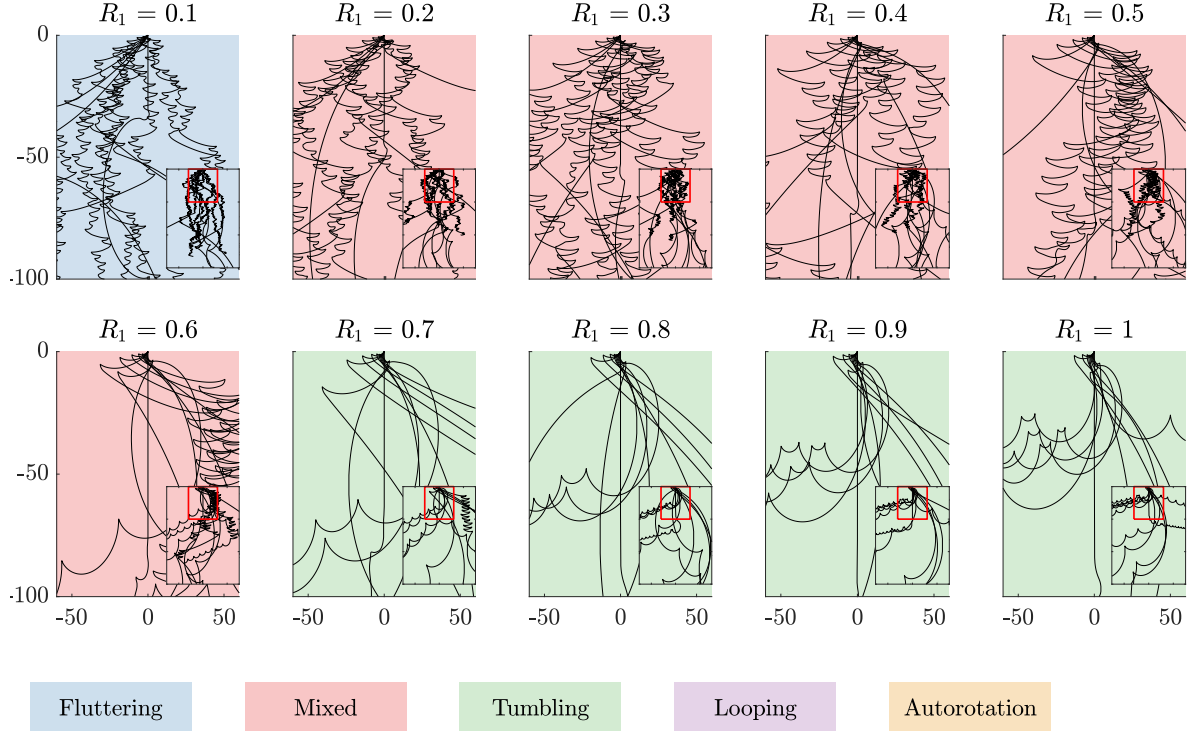


Figure 9: For $R_1 = 0.1, 0.2, \dots, 1$, snippets of the center-of-mass trajectories of falling plates for ten initial angles within $[0, \pi/4]$ during $0 \leq t \lesssim 500$. The plots are shaded according to the qualitative dynamics exhibited by the steady state. Each panel contains an inset that shows the large-scale features of the same trajectories, with a red rectangle indicating the portion shown in the main panel.

Alongside this large-amplitude fluttering, beginning at $R_1 \approx 0.2$ another falling motion emerges: tumbling. This transition is shown in panels $R_1 = 0.1$ and 0.2 of figure 9. The typical wake behind a tumbling trajectory is shown in figure 10, and can be seen more clearly in the supplementary movie “[movie_1.2_flatplate.avi](#)”. In this study, a plate is said to be tumbling if, like fluttering, the plate center-of-mass velocity vanishes periodically, but unlike fluttering, its angular velocity never changes sign. As for fluttering, cusps occur in the trajectories for tumbling when the center-of-mass velocity vanishes (e.g. figure 10(a)). As the density of the plate (R_1) increases, the fluid pressure force that restores the plate to the broadside-down position becomes insufficient to overcome the plate’s inertia. The plate thus falls end-over-end, and the trajectory is a series of curved arcs joined by cusps.

Figure 9 shows center-of-mass trajectories for plates with $0.1 \leq R_1 \leq 1$. Unlike the fluttering motions, whose amplitudes increase as R_1 increases (figure 9, $R_1 = 0.1, \dots, 0.5$), the amplitudes of the tumbling motions generally decrease as R_1 increases (figure 9, $R_1 = 0.6, \dots, 1$). Here, the fluttering amplitude refers to the mean distance traveled during each plate oscillation cycle, while the tumbling amplitude refers to the the mean distance traveled during each plate rotation cycle. While the fluttering motions are non-periodic and somewhat erratic, all the tumbling motions here are eventually periodic (as we can see from plots of the angular velocity versus time). There is an intuitive explanation for this difference. The dynamics of large clusters of vortices are inherently chaotic [Are83]. Typically the fluttering plate is close to a large cluster of vortices, and the non-periodicity of the plate motion seems to reflect that of the surrounding vortices. By contrast, a tumbling plate often moves away from its vortex wake into a smoother surrounding flow, allowing for more regular plate dynamics. This can also be seen from the numerical refinement study in appendix C which suggests that among all the falling motions observed, only the tumbling motions are *not* chaotic, in the sense that the other types of motion are highly sensitive to parameters. Within this transition regime, the plates can switch between fluttering and tumbling motions as can be seen in the inset of the $R_1 = 0.5$ panel in figure 9.

4.1.5 $0.7 \leq R_1 < 1.6$: the pure tumbling regime

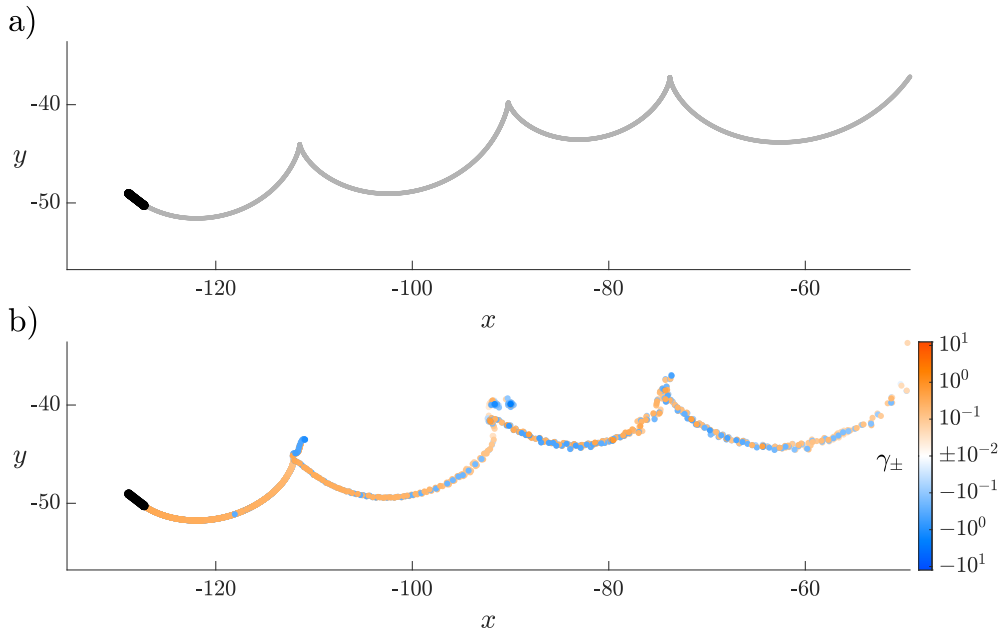


Figure 10: The trajectory of the center of mass (a) and the vortex wake (b) formed by a falling plate with $R_1 = 1$ undergoing tumbling.

Between $R_1 = 0.6$ and 0.7 , steady-state fluttering motions cease, and only tumbling motions remain. The transition between fluttering and tumbling was found at $I^* \approx 0.3$ in [Smi71] [Wan+16] [Soh24], which corresponds to $R_1 \approx 0.7$ here, since $I^* \approx \frac{4}{3\pi}R_1$ discussed in [Soh24]. It should be noted however, that unlike these other studies, here we consider a range of initial angles in $[0, \pi/4]$. The fact that the angular velocity of the plate undergoing a tumbling motion never changes sign is what distinguishes it from fluttering. Indeed, this is what is shown panel (b) of figure 10 with the bright orange (positive) vortex sheet released from the trailing edge of the plate as it tumbles. Unlike fluttering, in which vorticity is predominantly shed from the leading edge, in the tumbling motion vorticity is predominantly shed from the trailing edge. This may be one reason that although brief large-amplitude motions similar to looping and tumbling were found in a similar model without leading-edge shedding in [Soh24], no large-amplitude fluttering appeared.

Figure 10 shows that the maximum magnitude of vortex strength in the wake of a tumbling plate is only ≈ 10 . In contrast, figure 6 shows that for large amplitude fluttering the maximum vortex strength ≈ 1000 . Intuitively, the release of vorticity corresponds to a change in angular momentum of the plate. Hence, as the plate releases relatively little vorticity while tumbling, we might expect that it should travel with relatively constant angular velocity. If the plate travels approximately tangentially to its trajectory and has constant angular velocity, then the curvature of its trajectory would be relatively constant (i.e. it would resemble a circular arc). This is seen in figure 10 and more clearly in figure 11 where the curvature κ of the center-of-mass trajectory of a tumbling plate with $R_1 = 1.2$ is shown. The red dotted line at $\kappa = -0.125$ shows that for much of the tumbling period, the curvature is approximately constant. The large spikes in curvature mark the endpoints of each tumbling period, where a curvature singularity (i.e. a cusp) forms. In figure 12(a), the circular arcs formed by a tumbling plate's trajectory are also readily apparent.

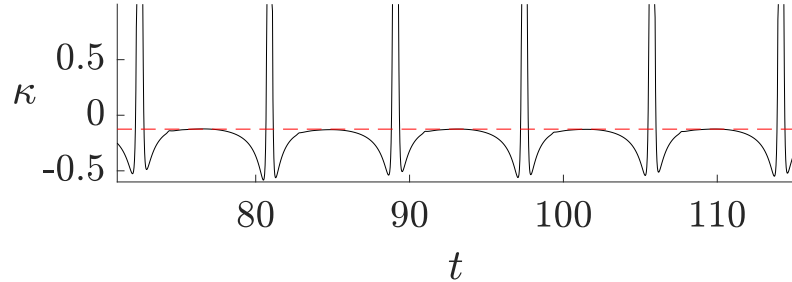


Figure 11: The curvature of the center-of-mass trajectory of a tumbling plate with $R_1 = 1.2$. The red dotted line at $\kappa = -0.125$ shows that the curvature within each tumbling period is relatively constant. The motion of this plate is shown in the supplementary movie “[movie_1.2.flatplate.avi](#)”.

As in the pure fluttering regime, tumbling motions may differ dramatically from one another. Near $R_1 = 1.4$, a special quasi-periodic tumbling motion occurs, shown in figure 12. For most initial angles, the plates tumble normally, forming the characteristic sharp cusps in their trajectories (figure 10). For apparently random initial angles, the plate overshoots as it falls, forming a loop as it tips over and slicing through its wake and trajectory. Despite the close interaction between the plate and its wake, the system remains quasi-periodic. In panel (a) we show the trajectory of the center of mass and the loops it forms, and in panel (b) we show a close-up of the plate configurations as it forms a loop. We number the first three snapshots

in red to indicate the direction of motion. In panels (c) and (d) respectively, we show the orientation angle and angular velocity, which is close to periodic.

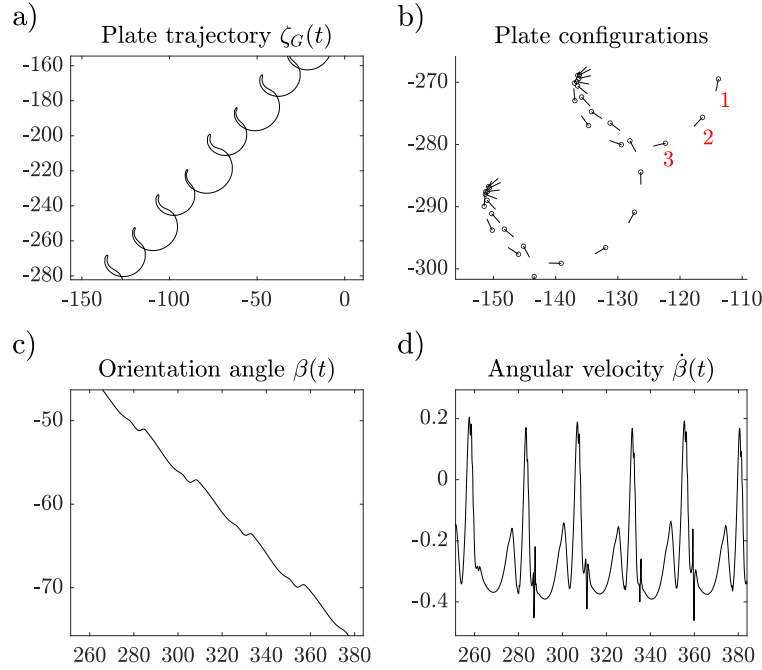


Figure 12: A special falling motion that occurs when $R_1 = 1.4$, for 5 out of 11 initial angles simulated. Instead of tumbling normally as in figure 10, the plate settles into a steady-state motion where it forms a loop at the tip of each tumbling arc, and alternates between smaller and larger loops. This falling motion appears near the transition between the tumbling and looping regimes, and blends the two falling motions.

4.1.6 $1.6 \leq R_1 < 2.8$: the looping regime

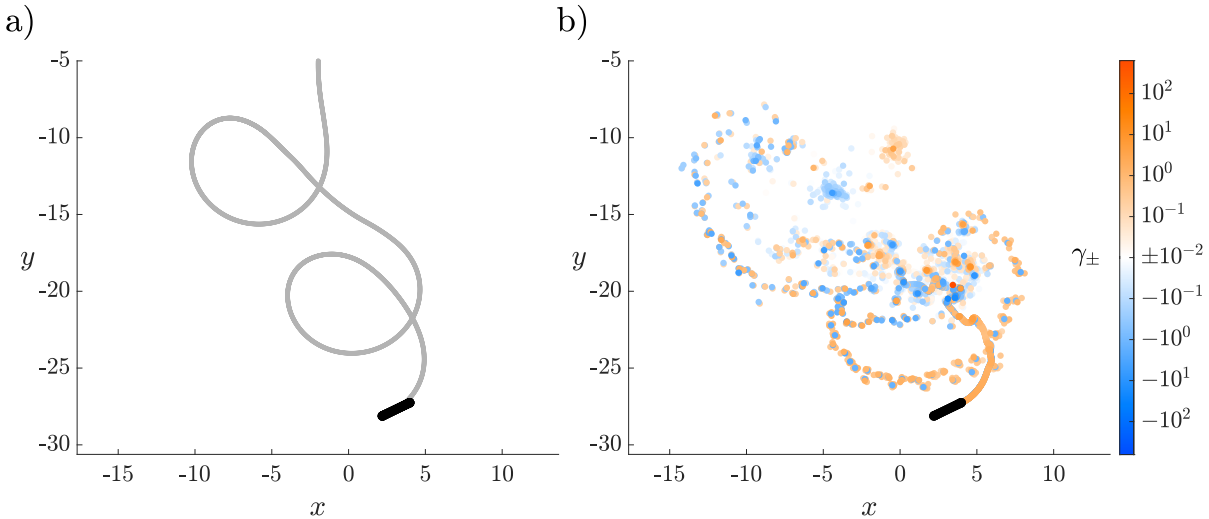


Figure 13: The trajectory of the center of mass (a) and the vortex wake (b) formed by a falling plate with $R_1 = 2.7$ undergoing a looping motion

As R_1 approaches 1.6, the stable periodic tumbling trajectories give way to erratic looping motions. Unlike tumbling motions, which do not change horizontal direction, these looping motions do, as in figure 13(a) where the trajectory shows loops. In this study, a plate is said to be undergoing a looping motion if its angular velocity never changes sign, but its horizontal velocity does. The fact that a looping body's horizontal velocity changes sign distinguishes it from tumbling. This motion resembles the “circling state” observed for falling flexible sheets [Alb10a]. There, the flexible body bends into a circular arc with curvature approximating that of its looping trajectory. By conforming its body curvature to its trajectory, the flexible body is able to stabilize this falling motion. Instead of looping chaotically, the flexible body instead loops in a quasi-periodic fashion for extended time periods. As R_1 increases in the range [1.6, 2.8], the loop radius shrinks (figure 14, $R_1 = 1.9, 2.2, 2.5, 2.8$) until the plate begins to autorotate.

The transition between looping and autorotation is shown by motions at a sequence of R_1 values in figure 15. Here we define autorotation as a plate motion in which both angular and horizontal velocities never change sign. The single-signed horizontal velocity distinguishes autorotation from tumbling and looping. At $R_1 = 2.7$ (second row of figure 15), near the transition between fluttering and tumbling, the horizontal velocity $\dot{x}_G(t)$ (right column) oscillates with a single sign for much of the first half of the time series (autorotation) but often reverses sign during the second half (looping). When $R_1 > 2.8$ (figure 15, $R_1 = 3, 3.4$) the $\dot{x}_G(t)$

time series is single-signed, showing autorotation only. As R_1 increases within this regime, the time-averaged horizontal velocity magnitude also increases.

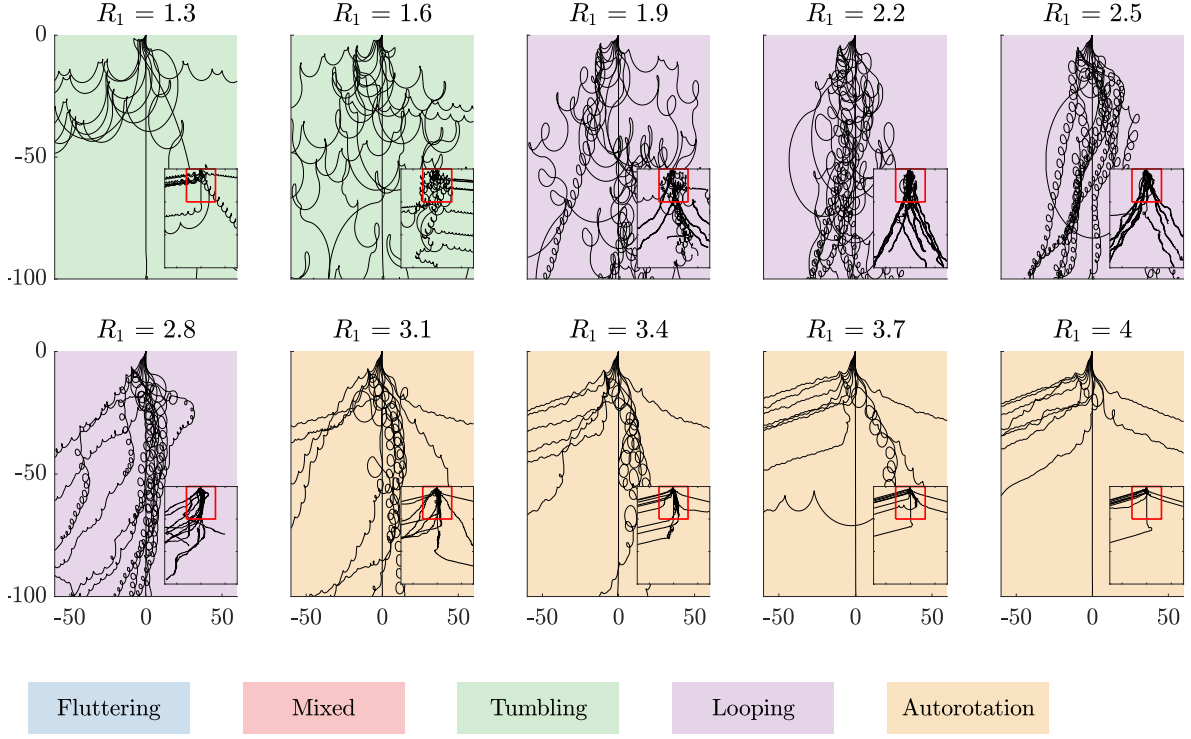


Figure 14: For $R_1 = 1.3, 1.6, \dots, 4$, snippets of the center-of-mass trajectories of falling plates for ten initial angles within $[0, \pi/4]$ during $0 \leq t \lesssim 500$. The plots are shaded according to the qualitative steady-state dynamics. In each panel an inset shows the large-scale features of the trajectories, with a red rectangle indicating the region shown in the main panel.

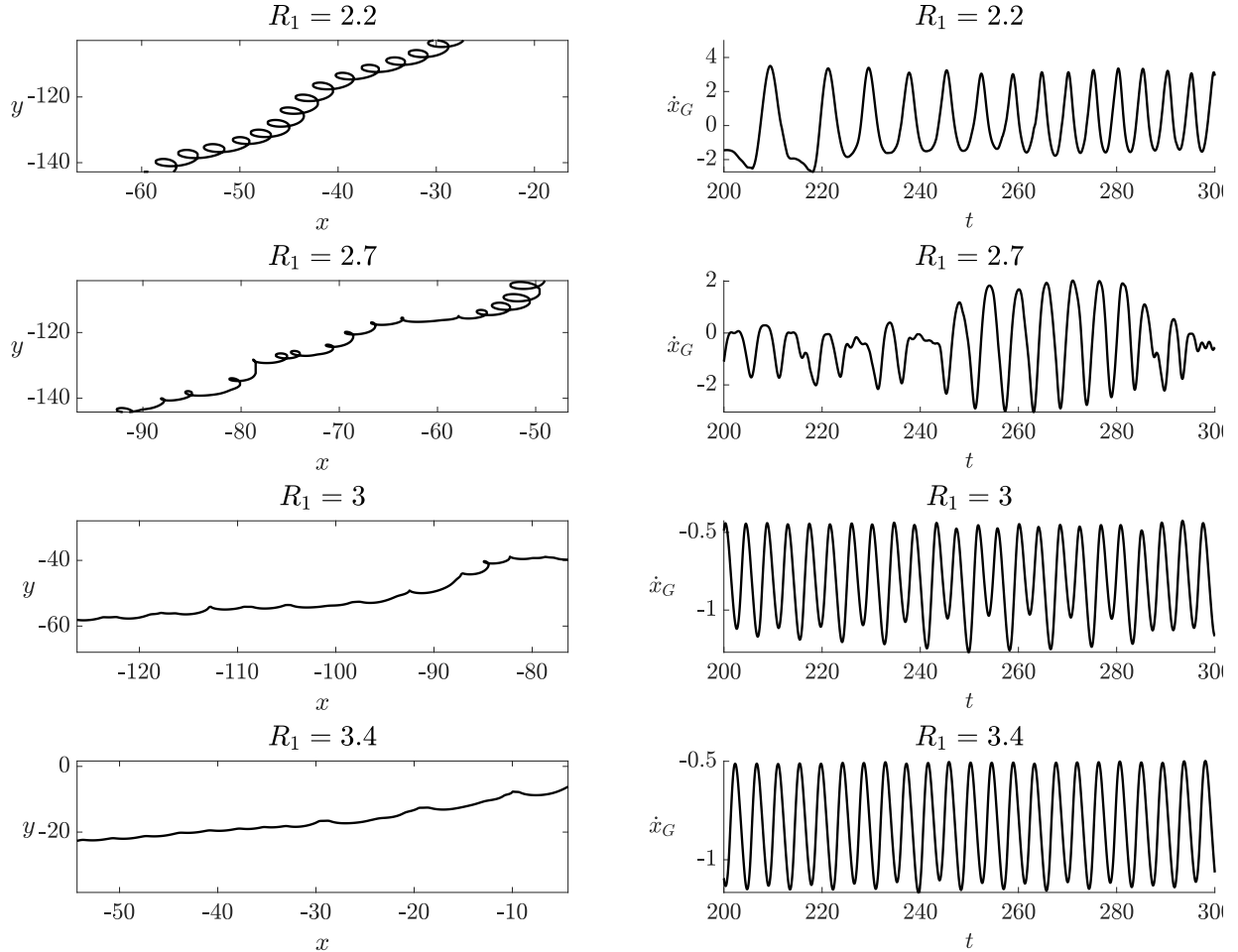


Figure 15: Motions at $R_1 = 2.2, 2.7, 3, 3.4$ showing the transition between looping and autorotation. Left column: snippets of center-of-mass trajectories. Right column: time series of horizontal velocity $\dot{x}_G(t)$.

4.1.7 $2.8 < R_1$, The autorotation regime

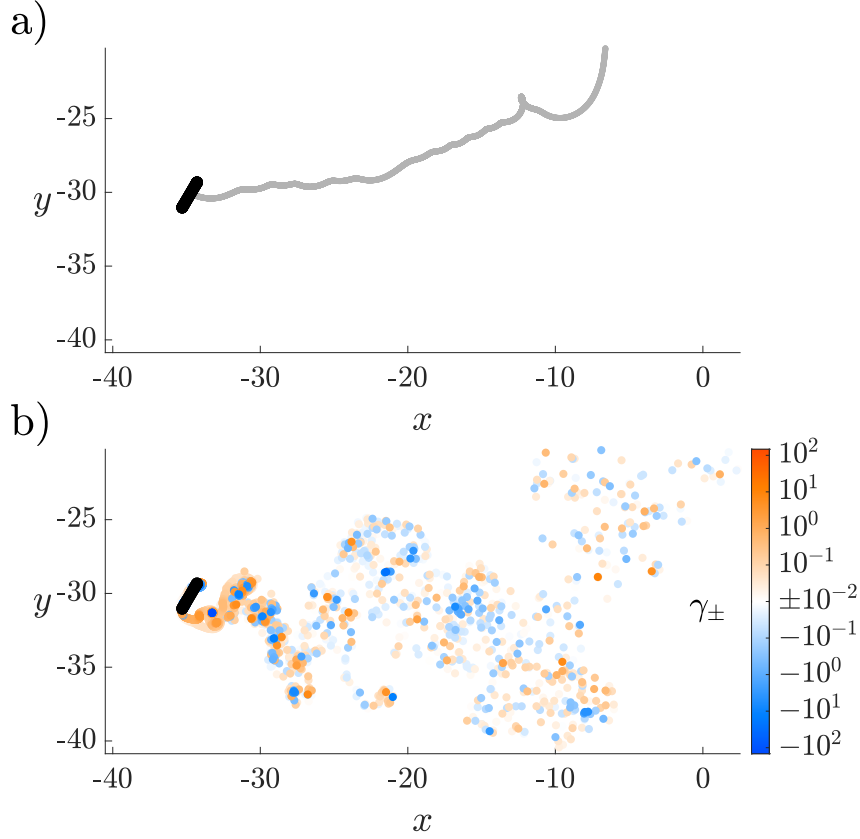


Figure 16: The center-of-mass trajectory (a) and vortex wake (b) of an autorotating plate with $R_1 = 4$.

For $R_1 > 2.8$ the plate primarily autorotates quasiperiodically. The typical vortex wake behind an autorotating plate is shown in figure 16. In figure 17 we show the effect of increasing R_1 from 10 to 1000, within the autorotation regime. In this wide range of R_1 the plates reach similar steady-state trajectories, shown in panel (a) (except for $R_1 = 1000$, not yet at steady state). Panel (b) shows that shortly after being released from rest ($t \approx 0.1$ –1), the plates' angular velocity magnitudes increase as a power law $\propto t^3$ before saturating at $O(1)$ values across all tested R_1 values. The duration of the transient growth phase increases with increasing R_1 . In the saturated regime, the angular velocity magnitude has oscillations whose amplitudes decrease with R_1 (as shown in panel (c)), but whose time averages are approximately 0.65, independent of R_1 in this regime.

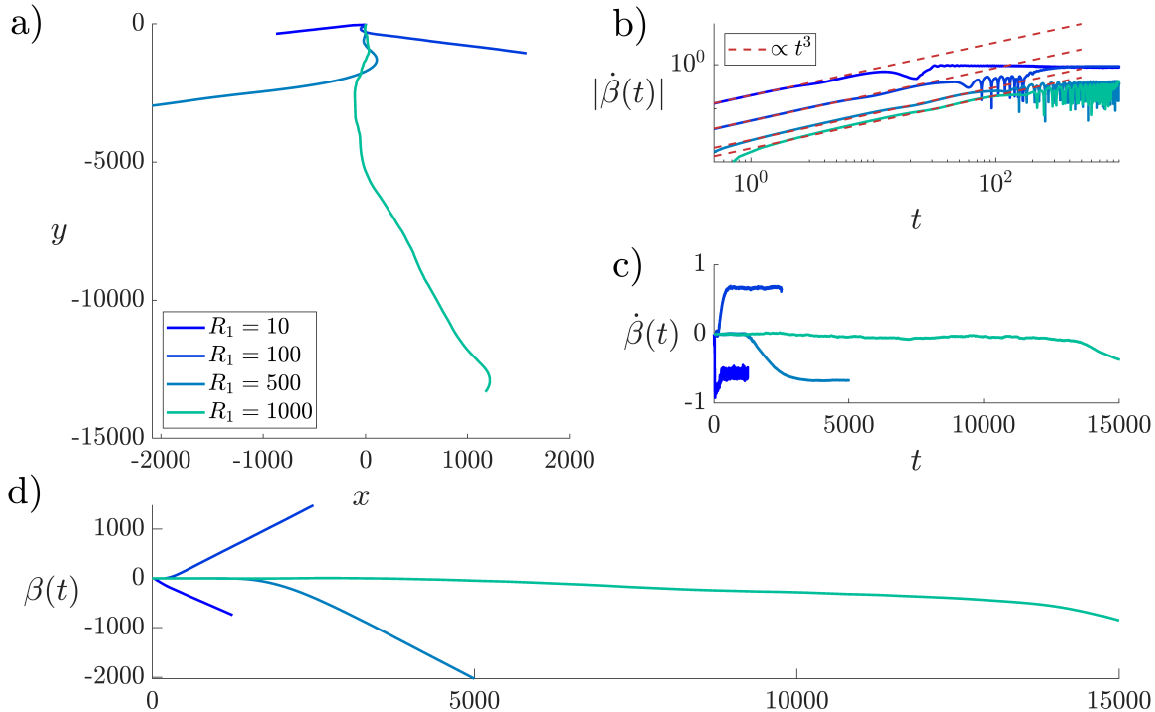


Figure 17: (a) The trajectory of the center of mass $\zeta_G(t)$, (b) angular velocity magnitude $|\dot{\beta}(t)|$ on logarithmic scale with red dotted lines showing curves proportional to t^3 , (c) the angular velocity, and (d) the orientation angle $\beta(t)$ of falling plates released at a fixed initial angle with $R_1 = 10, 100, 500, 1000$.

4.2 V-shaped plates

4.2.1 The effect of bending angle

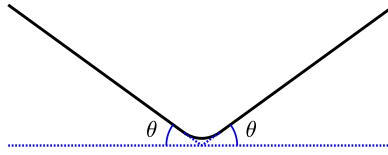


Figure 18: Illustration of the bending angle θ .

Having observed the effect of R_1 on the qualitative dynamics of falling flat plates, we extend our study to curved plates. Such a transformation breaks the \pm symmetry of the plate and introduces new falling dynamics while suppressing others. We consider a one-parameter family of bent, V-shaped plates indexed by θ , the bending angle shown in figure 18. The sharp tip of the V shape is smoothed by replacing it with a circular arc with radius $\frac{2}{5\pi}$. The bending angle θ is equal to half the exterior angle of the plate. This class of plates is unable to move in a purely tangential motion, so we now omit skin friction, which was introduced to suppress such motions for the flat plate. The results in what follows are drawn from the analysis of ≈ 1000 simulations up to $t \approx 500$. In table 4 we summarize the numerical parameters considered in this portion of the study.

Initial angles	$0^\circ, 4.5^\circ, 9^\circ, 13.5^\circ, \dots, 45^\circ$
R_1	$0, 0.1, \dots, 1, 2, \dots, 5$
θ	$11.25^\circ, 15.47^\circ, 19.69^\circ, 23.91^\circ, 28.12^\circ, 32.34^\circ, 36.56^\circ, 40.78^\circ, 45^\circ$

Table 4: Table showing the values of the physical parameters being varied for the falling V-plates

In figure 19, we show the center-of-mass trajectories of various falling V-shaped plates for $0 \leq t \leq 500$. Each column corresponds to a single value of $R_1 \in [0.1, 0.9]$, with the bending angle θ (listed at the bottom left of each panel) increasing downward. For these small values of R_1 , the flattest plates ($\theta \leq 11.3^\circ$) behave chaotically, forming loops due to the absence of skin friction in the model. The more bent plates typically flutter instead, with quasi-periodic and sometimes periodic dynamics. The periodic dynamics correspond to approximately straight-line trajectories (e.g. $R_1 = 0.9$, $\theta = 28.1^\circ$). During each period, the body travels fixed distances d_v and d_h in the vertical and horizontal directions, yielding a straight-line path with slope d_v/d_h .

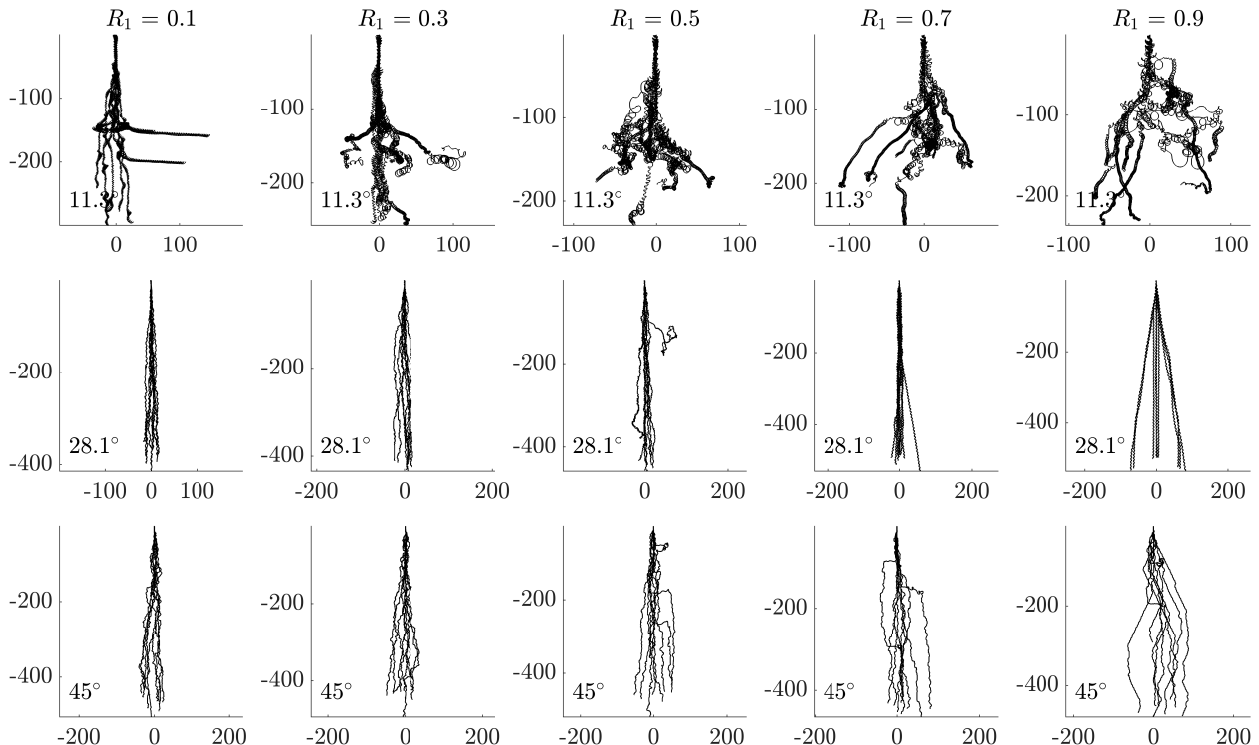


Figure 19: The center-of-mass trajectories of falling bent plates for $0 \leq t \leq 500$, $R_1 = 0.1, 0.3, \dots, 0.9$, and bending angles $11.3^\circ, 28.1^\circ$, and 45° .

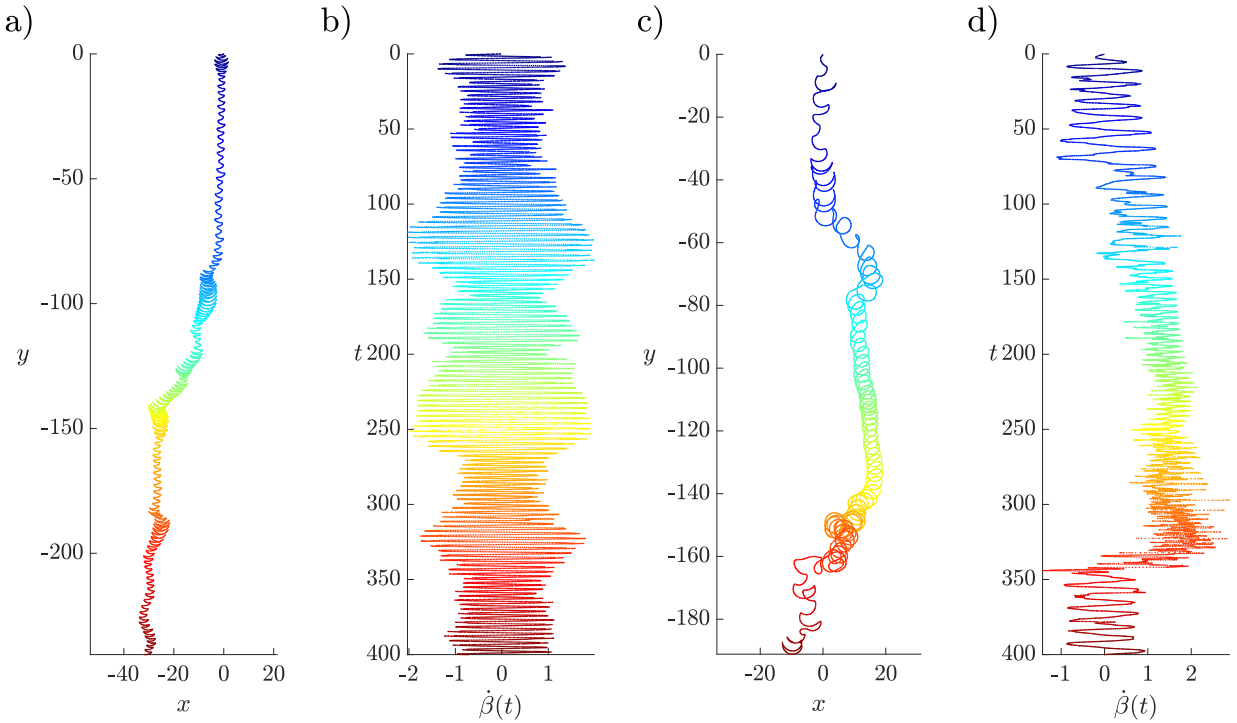


Figure 20: (a),(c) Center-of-mass trajectories and (b),(d) angular velocities of V-shaped plates with densities $R_1 = 0.1$ and 0.7 respectively, and bending angle $\theta = 11.3^\circ$, for $0 \leq t \leq 400$. In each panel, the colors correspond to time, with the mapping given by the vertical axes of panels (b) and (d).

For small R_1 , the plate flutters for a range of $\theta \leq 11.3^\circ$, as in figure 19 as well as figure 20(a). In this figure, we compare the center-of-mass trajectories (panels (a) and (c)) and the angular velocities (panels (b) and (d)) for plates with $R_1 = 0.1$ and 0.7 , and bending angle 11.3° . The plots are colored by time t . Interestingly, the bent plates flutter with an angular velocity whose amplitude varies in time, as shown in panel (b). By contrast, the angular velocity amplitude is approximately constant for flat-plate fluttering. For the example in figure 20(b), the angular velocity amplitude is small near $t = 50$ (i.e. slow fluttering) and large near $t = 125$ (i.e. fast fluttering). The gradual increase in angular velocity from $t = 50$ to 125 corresponds to the accumulation of vorticity behind the plate. This can be seen more clearly in the supplementary movie “[movie_0.1_11.3_vplate.avi](#)”. In response, the plate oscillates faster and faster until it escapes from its wake, and then flutters slowly again near $t = 160$ before repeating the process, alternating between slow and fast fluttering at irregular time intervals.

As R_1 increases past 0.2 , the fluttering amplitude increases until the plate begins to overturn and then loop chaotically, as shown in figure 20(c). Without the restoring force of skin friction that stabilizes the fluttering motion, the V-shaped plates loop instead of flutter as the flat plates do. In summary, for V-shaped plates with $\theta \leq 11.3^\circ$, the fluttering state is inherently stable for $R_1 \leq 0.1$, but for larger values of R_1 fluttering is unstable without skin friction. Sometimes, the looping plate spontaneously returns to fluttering, as shown at $t \approx 350$ in figure 20(c).

The tumbling motion (falling end-over-end), which occurred for the flat plate when $0.2 < R_1 < 1.7$, does not occur for the bent plates. This may be because the bent plate is not symmetric after a 180° rotation, so the fluid forces would be greatly altered on each half-cycle of a tumbling motion (which does not arise). On the other hand, the bent plate has bilateral symmetry about the plate midpoint. A side-to-side fluttering motion has a similar symmetry in the fluid forces between times when the plate moves to one side and to the other, which may be one reason that symmetric fluttering can occur for V-shaped plates. Unlike the bent plates, The mirror and 180° symmetries of the flat plate may allow it to perform *both* fluttering and tumbling motions.

Figure 21 is analogous to figure 19 except with larger $R_1, \in [1, 5]$. In this R_1 range, the plates with small bending angle (top row) transition from chaotic motions at smaller R_1 to periodic autorotating motions at larger R_1 . However, for larger bending angles (second and third rows), the plates transition from quasi-periodic fluttering at smaller R_1 to chaotic motions at larger R_1 . In the supplementary movie “[movie_5_11.3_vplate.avi](#)” the periodic autorotation of a V-shaped plate at large R_1 can be seen.

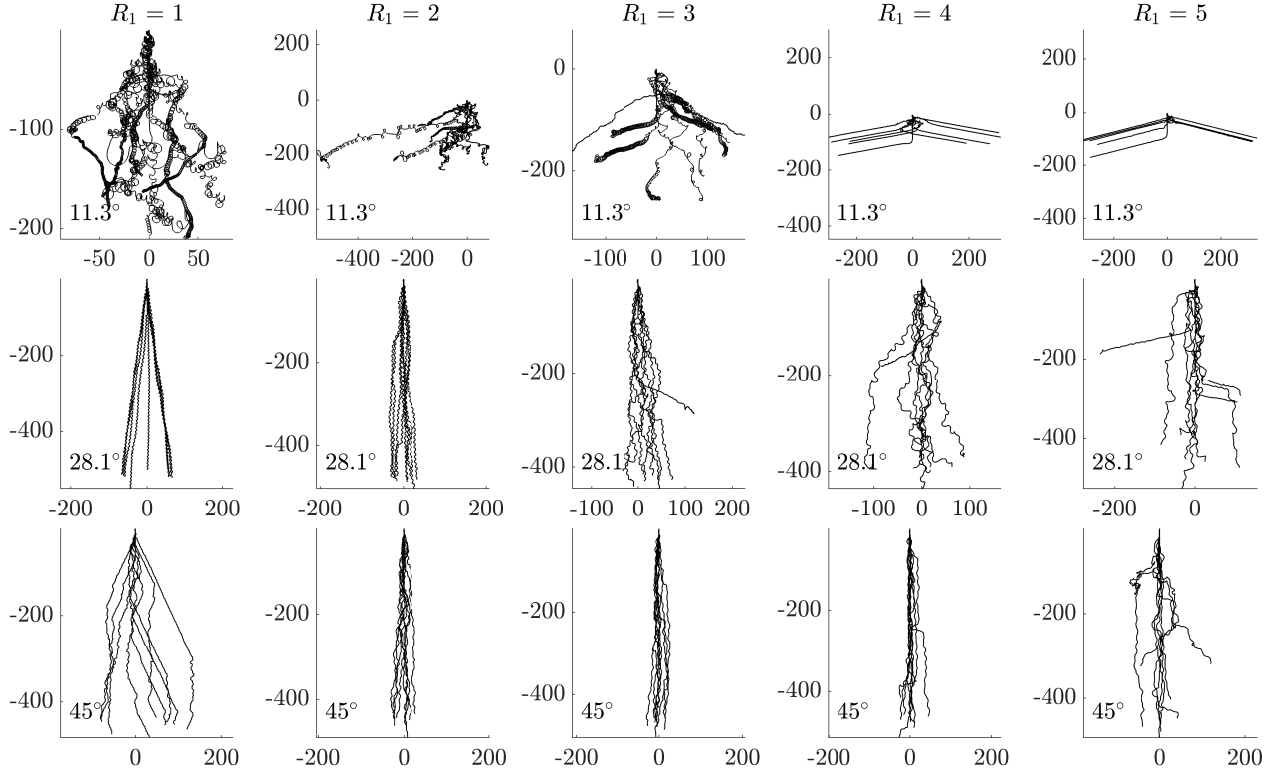


Figure 21: The trajectories of falling bent plates up to $t \approx 500$ for $R_1 = 1, 2, \dots, 5$ (one per column) and bending angles $\theta = 11.3^\circ, 28.1^\circ, 45^\circ$ (one per row, shown at the bottom left of each panel).

An important quantity that varies strongly among the falling motions is the plate's average speed. This is shown by the heat maps of figure 22, in the space of R_1 and the bending angle θ . Generally, white, yellow, and orange correspond to (fast) chaotic looping motions, dark red corresponds to (slower) periodic fluttering, and (even slower) black corresponds to periodic autorotation. The regions of relatively constant speeds $\approx 1 - 1.2$ for larger θ and R_1 have similar slow fluttering motions. The heatmap in figure 22 thus represents a phase diagram of the falling V-shaped plates. The proximity of the average speeds to 1 is consistent with our nondimensionalization, which used an estimate of the terminal velocity as the characteristic speed.

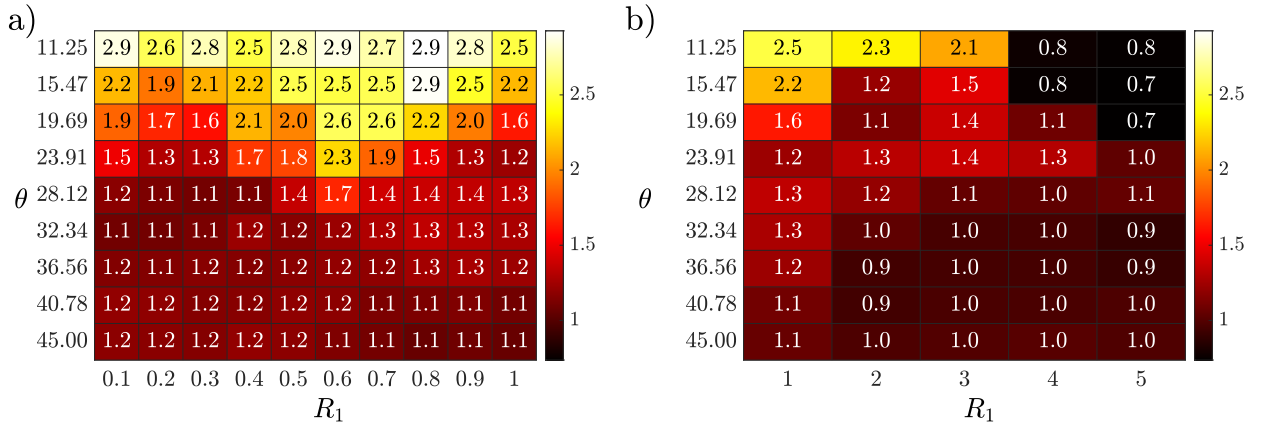


Figure 22: Heat maps showing the average center-of-mass speed versus R_1 and bending angles θ for the bent plates, with $0.1 \leq R_1 \leq 1$ (a) and $1 \leq R_1 \leq 5$ (b).

4.2.2 Obtuse fluttering



Figure 23: Snapshots of a V-shaped plate in obtuse fluttering with bending angle $\theta = 28.1^\circ$ and $R_1 = 0.9$.

Most of the bent-plate dynamics were also seen for the flat plate. Here we show a distinct bent-plate motion that we call “obtuse fluttering,” shown in figure 23 at $R_1 = 0.9$ and $\theta = 28.1^\circ$. This fluttering motion has cusps with obtuse rather than acute angles (as seen for the flat plate, e.g. figures 3–6), because the plate begins to overturn slightly at each cusp, with orientation angle magnitude $|\beta|$ peaking slightly above 90° . With obtuse angles the trajectory appears smoother than those for flat-plate fluttering.

Unlike the fluttering motions of the flat plate, which are nonperiodic, this bent-plate fluttering motion is periodic. Without the rotational symmetry of the flat plate, the bent plate flutters through a substantially different mechanism. At $R_1 = 0.9$, the flat plates exhibit tumbling rather than fluttering because plate inertia is large relative to the restoring force of fluid pressure. However, bent plates experience very different fluid forces in an upside-down-V position (\wedge). Previous experiments [CVZ06] [Ami+19] and figure 24 indicate that such a position is unstable and this may inhibit tumbling and stabilize the fluttering state. Supplementary movie “[movie_0.9_28.1_vplate.avi](#)” shows an obtuse fluttering motion.

We illustrate the physical mechanism preventing overturning in figure 24 by plotting the orientation angle β , angular velocity $\dot{\beta}$ and angular acceleration $\ddot{\beta}$ (panel (a)) and the rates of change of the circulation magnitudes of the \pm vortex sheets (panel (b)) for the obtuse fluttering plate in figure 23.

When $t \approx 164$ in figure 24(a), β has a maximum. The plate has rotated by a little more than $+\pi/2$ radians and the $+$ edge is trailing. At the same time, $t \approx 164$, in panel (b), the rate of change of circulation in the $+$ sheet is zero. In general, at the start of each half-period when β has a maximum/minimum, no vorticity is released at the trailing edge. The restoring force inducing this obtuse fluttering motion thus appears to be primarily due to vorticity released at the leading edge. Panel (a) shows that, like a harmonic oscillator, the sign of $\ddot{\beta}$ (and therefore the torque) is opposite to the sign of the orientation angle. In other words, the fluid always applies a torque to the bent plate that restores it to the \vee position with its tip pointed downward. When the plate overturns (i.e. its angle magnitude exceeds 90°), there is a small local jump in torque corresponding to a sudden increase in restoring force. Note that when $\pm\beta < 0$, the \pm edge is leading. At these times in panel (b), the rate of change of the magnitude of circulation in the \pm sheet is positive, so circulation on the \pm edge is increasing. During the sub-period where it is trailing, the circulation on the \pm sheet decreases. Over each period however, the magnitude of circulation on each sheet has a net increase. Intuitively, this corresponds to the transfer of gravitational potential energy to the kinetic energy of the fluid.

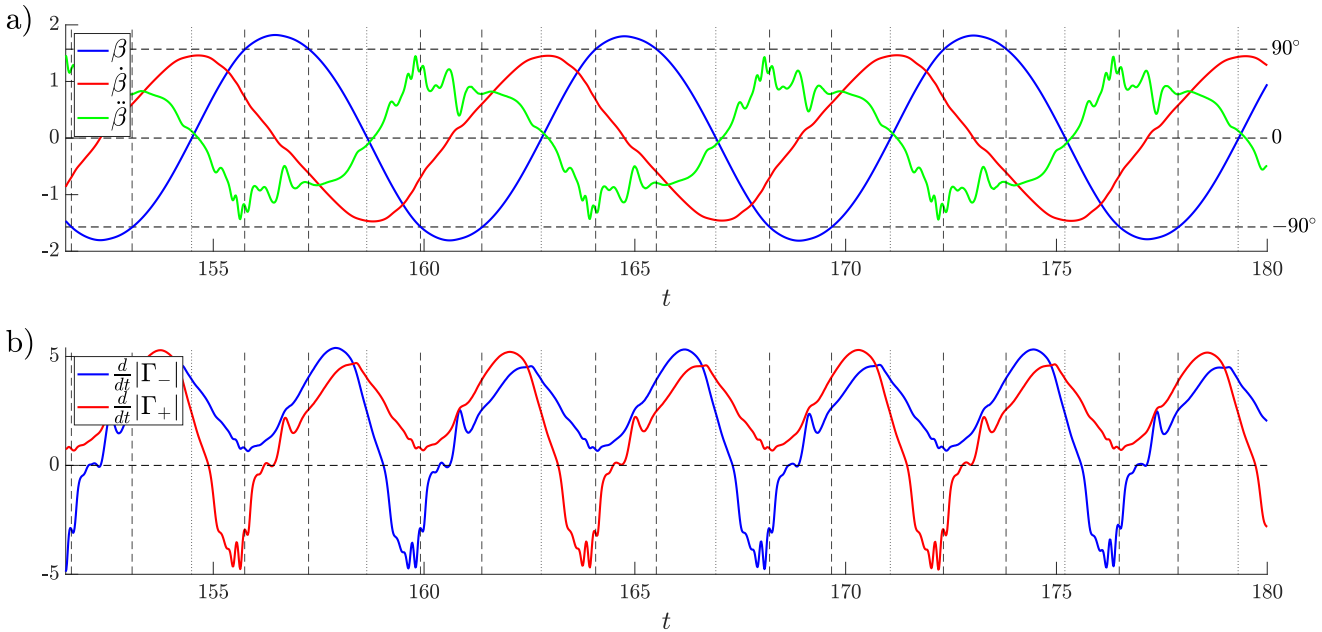


Figure 24: (a) The orientation angle β (blue), angular velocity $\dot{\beta}$ (red) and angular acceleration $\ddot{\beta}$ (green) for a V-shaped plate in an obtuse fluttering motion with bending angle $\theta = 28.1^\circ$ and $R_1 = 0.9$. (b) The rate of change of the magnitude of the circulation of the \pm sheet shown in red and blue respectively.

4.2.3 $R_1^{-\frac{1}{2}}$ -scaling of the dominant angular momentum frequency

The generic behavior of the plates with large bending angles, $\theta > 28.12^\circ$, is quasi-periodic fluttering. We can quantitatively study the effect of R_1 on the fluttering frequency of these bent plates. To estimate the fluttering frequency, we take the Fourier transform of the angular momentum, and locate the frequency f_{max}

that maximizes the power spectrum, and average over all initial release angles. For all fluttering motions, a power law with exponent $-\frac{1}{2}$ shows good agreement with the data when $R_1 \leq 1$. (See figure 25). This scaling law was obtained for flat plates via dimensional analysis in [BEM98]. Bending the plates extends the range of R_1 where fluttering occurs to larger values, extending the range of validity of this scaling law. A similar scaling law is reported in [MA20] for the oscillation frequency of a thin membrane in inviscid flow.

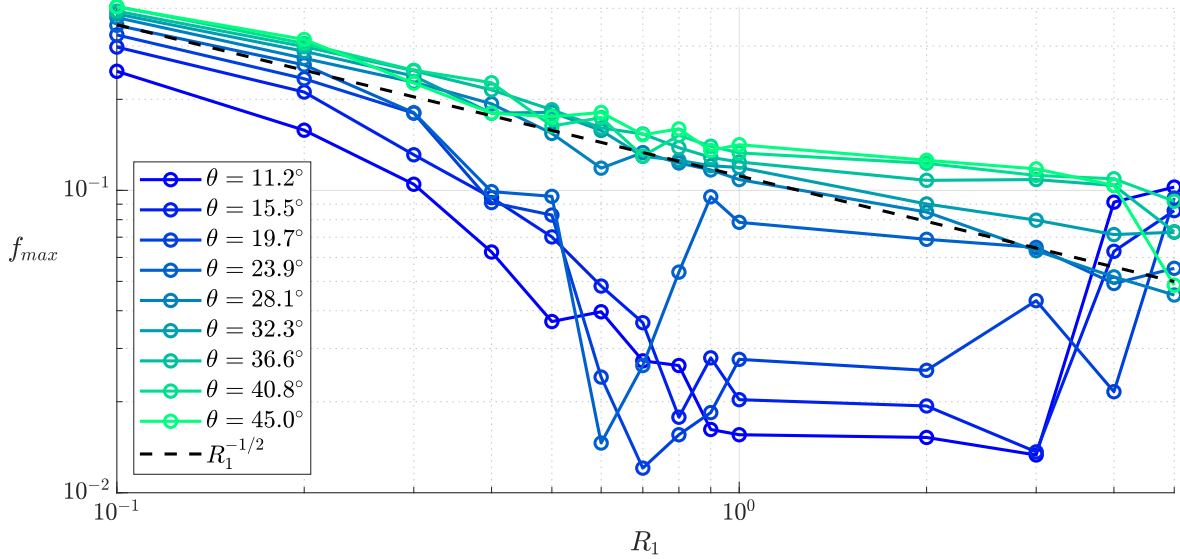


Figure 25: Log-log plot of the maximum frequency f_{max} against R_1 . For $\theta \geq 28.1^\circ$ and $R_1 \leq 1$ the generic falling motion is fluttering with a frequency that scales as $R_1^{-\frac{1}{2}}$.

In figure 26 we represent the data in figure 25 as a heat map analogous to figure 22. As before, the sharp changes in peak frequency (and color) represent sharp changes in the falling motion. The looping motions are predominantly aperiodic and have darker colors. On the other hand, low density, highly bent plates flutter rapidly, and have lighter colors. The sharp increase in f_{max} for $\theta \leq 15.47^\circ$ when R_1 increases from 3 to 4 corresponds to the transition to autorotation, as can be seen in the first row of figure 21. The heat map of frequency in figure 26 sketches the phase diagram of falling motions of V-shaped plates and the sharp jumps in value are generally consistent with the similar sketch shown by the heat map of average speed in figure 22. However, some phase transitions are better captured by the heat map of average peak frequency. For example, when $\theta = 11.25^\circ$, as R_1 transitions from 0.1 to 0.2 the peak frequency drops from 0.25 to 0.16 suddenly. This corresponds to the transition from small amplitude fluttering to looping. By contrast, in figure 22, the average speed transitions smoothly from 2.9 to 2.6 over the same R_1 and θ values. Similarly, when $\theta = 45^\circ$, as R_1 transitions from 4 to 5 the peak frequency f_{max} jumps from 0.1 to 0.05 while the average center-of-mass speed remains constant at 1. This transition can also be seen in the last row of columns $R_1 = 4, 5$ in figure 21. From the center-of-mass trajectories shown in the figure, it can be seen that at $R_1 = 5$, the trajectories are noticeably more erratic than at $R_1 = 4$. This corresponds to more overturning and longer phases of autorotation at $R_1 = 5$ than at $R_1 = 4$. The heat map of average center-of-mass speed thus sketches a phase diagram of lower resolution than that of the heat map of average peak frequency.

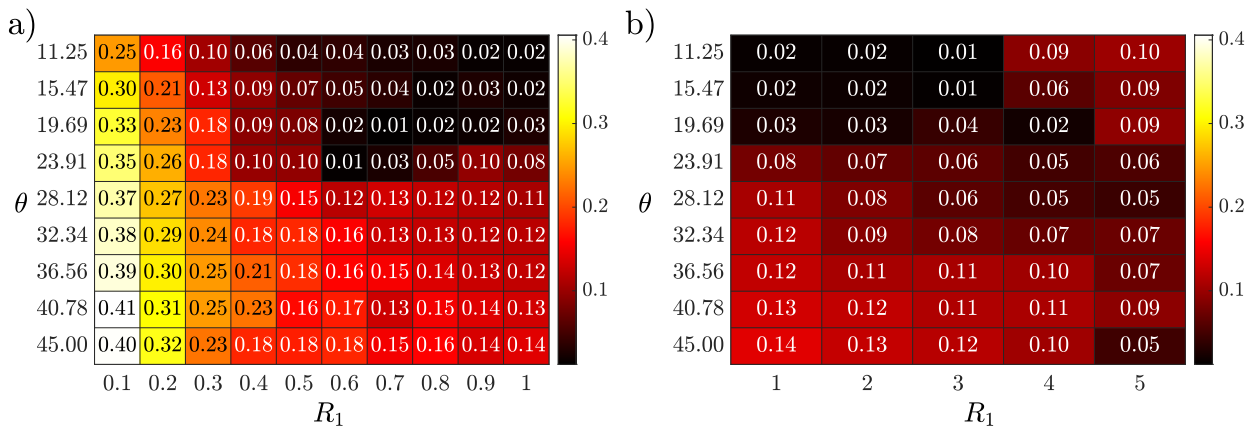


Figure 26: Heat maps of average peak frequency versus R_1 and θ for bent plates with (a) $0.1 \leq R_1 \leq 1$ and (b) $1 \leq R_1 \leq 5$.

5 Conclusion

We demonstrated a new numerical model for falling bodies that includes the leading-edge shedding of vorticity. The inclusion of leading-edge vortex shedding allows for more realistic dynamics in the vortex sheet simulations of falling plates. It allows for long-time fluttering and tumbling dynamics previously only observed in direct Navier-Stokes simulations and experiments, while also predicting other falling motions that could potentially be observed in experiments. Some interesting special fluttering motions were observed, such

as the progressive fluttering observed in [PR24] and the obtuse fluttering of the V-shaped plates. This obtuse fluttering is characterized by obtuse-angled cusps in the trajectory, and is driven primarily by leading-edge shedding effects, which provide a restoring force to the V position with sign opposite to that of the plate orientation angle. For flat plates at low values of R_1 fluttering motions dominate. As R_1 increases, the dominant motion transitions to tumbling, looping, and then autorotation at key transition values. The transition between fluttering and tumbling dynamics observed at $R_1 \approx 0.7$ (equivalently, $I^* \approx 0.3$) is consistent with several prior experimental and viscous numerical investigations. While the amplitude of side-to-side fluttering motions increases with increasing R_1 , the amplitude of tumbling motions decreases. For small R_1 , bending the plate stabilizes its motion, yielding quasi-periodic instead of chaotic fluttering, while for large R_1 , bending the plate destabilizes it from quasi-periodic autorotation to chaotic fluttering. When $\theta > 28.12^\circ$ only fluttering modes are observed, with frequencies that scale as $R_1^{-\frac{1}{2}}$ when $R_1 \leq 1$.

Acknowledgments

This research was supported by the NSF-DMS Applied Mathematics program under award number DMS-2204900.

A The logarithmic singularity

Here we rigorously justify the presence of the logarithmic singularities at the endpoints of the Cauchy integral

$$\frac{1}{2\pi i} \int_{-1}^1 \frac{\gamma_b(s, t)}{z - \zeta(s, t)} ds. \quad (54)$$

The results found here are well known, and can be found in much greater generality in [Mus58]. For completeness however, we provide simpler arguments using only standard complex analysis. We require only a very weak form of the Sokhotski-Plemelj formula which can be stated as follows. Given any C^1 (continuously differentiable) curve C and C^1 function $g(z)$ on the complex plane, then for any interior point $c \in C$, we have:

$$\lim_{z \rightarrow c^\pm} \frac{1}{2\pi i} \int_C \frac{g(\zeta)}{\zeta - z} d\zeta = \frac{1}{2\pi i} \int_C \frac{g(\zeta)}{\zeta - c} d\zeta \pm \frac{1}{2} g(c).$$

Here the \pm superscript indicates the side from which $c \in C$ is approached. Under these stronger assumptions, this formula is immediate. Indeed, when $g(z) \equiv 1$ we may integrate exactly, and obtain the formula via contour integration. Fix c , an interior point of C , and let C_ϵ be the curve C after removing a symmetric segment of length ϵ centered at c . Observe that:

$$\begin{aligned} \lim_{z \rightarrow c^\pm} \frac{1}{2\pi i} \int_C \frac{g(\zeta)}{\zeta - z} d\zeta &= \lim_{z \rightarrow c^\pm} \frac{1}{2\pi i} \int_C \frac{g(\zeta) - g(z)}{\zeta - z} d\zeta + \lim_{z \rightarrow c^\pm} g(z) \frac{1}{2\pi i} \int_C \frac{1}{\zeta - z} d\zeta \\ &= \frac{1}{2\pi i} \int_C \frac{g(\zeta) - g(c)}{\zeta - c} d\zeta + g(c) \frac{1}{2\pi i} \int_C \frac{1}{\zeta - c} d\zeta \pm \frac{1}{2} g(c) \\ &= \lim_{\epsilon \rightarrow 0} \frac{1}{2\pi i} \int_{C_\epsilon} \frac{g(\zeta) - g(c)}{\zeta - c} d\zeta + g(c) \frac{1}{2\pi i} \int_C \frac{1}{\zeta - c} d\zeta \pm \frac{1}{2} g(c) \\ &= \frac{1}{2\pi i} \int_C \frac{g(\zeta)}{\zeta - c} d\zeta - g(c) \frac{1}{2\pi i} \int_C \frac{1}{\zeta - c} d\zeta + g(c) \frac{1}{2\pi i} \int_C \frac{1}{\zeta - c} d\zeta \pm \frac{1}{2} g(c) \\ &= \frac{1}{2\pi i} \int_C \frac{g(\zeta)}{\zeta - c} d\zeta \pm \frac{1}{2} g(c). \end{aligned}$$

The second equality follows from the fact that $|\frac{g(\zeta) - g(z)}{\zeta - z}| \leq \max_{\zeta \in C} (\|\nabla g(\zeta)\|)$ (which exists as $g \in C^1$), and dominated convergence. The third equality is a consequence of dominated convergence as well, while the fourth follows from the definition of the principal valued integral.

We now turn our attention to (54) and begin the argument. Recall that $\zeta(s, t)$ parameterizes the curve representing the thin plate in the complex plane. Let C_b denote this curve, and let $c_\pm = \zeta(\pm 1, t)$ denote its endpoints. Let us focus on the positive edge c_+ and define the function

$$g(\zeta(s, t)) = \gamma_b(s, t) \overline{\partial_s \zeta(s, t)}.$$

Notice that

$$|g(c_\pm)| = |\gamma_b(\pm 1, t)|.$$

Hence g vanishes at the endpoints if and only if γ_b does. Let $w = \zeta(s, t)$. Then we may rewrite the

contribution of the body to the conjugate fluid velocity as

$$\begin{aligned}
\int_{-1}^1 \frac{\gamma_b(s, t)}{z - \zeta(s, t)} ds &= \int_{C_b} \frac{g(w)}{z - w} dw = \int_{C_b} \frac{g(w) - g(c_+) - \nabla g(c_+) \cdot (w - c_+)}{z - w} dw \\
&\quad - g(c_+) \int_{C_b} \frac{dw}{w - z} - \nabla g(c_+) \cdot \int_{C_b} \frac{w - c_+}{w - z} dw \\
&= \int_{C_b} \frac{g(w) - g(c_+) - \nabla g(c_+) \cdot (w - c_+)}{z - w} dw \\
&\quad - g(c_+) (\log(c_+ - z) - \log(c_- - z)) \\
&\quad - \nabla g(c_+) \cdot \left(c_+ - c_- + (z - c_+) (\log(c_+ - z) - \log(c_- - z)) \right) \\
&=: I_1 + I_2 + I_3.
\end{aligned}$$

Clearly, $I_3 = \Theta(1)$ as $z \rightarrow c_+$. If $\gamma_b(1, t) = 0$, then $g(c_+) = 0$, in which case $I_2 = 0$. When $\gamma_b(1, t) \neq 0$ however, $I_2 = \Theta(\log(c_+ - z))$ as $z \rightarrow c_+$. The first term, I_1 , however, requires a more careful analysis. First, we observe that we may extend the body C_b along the positive edge linearly so that it remains a C^1 curve which we call C_b^{ext} . Let $h(w) = g(w) - g(c_+) - \nabla g(c_+) \cdot (w - c_+)$. Then $h(c_+) = 0$ and $\nabla h(c_+) = 0$ automatically. Therefore, by letting h vanish on the extended part of the body, h admits a C^1 extension to the new body C_b^{ext} such that we may write

$$I_1 = \int_{C_b} \frac{h(w)}{z - w} dw = \int_{C_b^{\text{ext}}} \frac{h(w)}{z - w} dw. \quad (55)$$

The point of this is that now c_+ is an interior point of the curve C_b^{ext} , so that the Sokhotski-Plemelj formulae apply. Hence,

$$\lim_{z \rightarrow c_+} \int_{C_b^{\text{ext}}} \frac{h(w)}{z - w} dw = \int_{C_b^{\text{ext}}} \frac{h(w)}{c_+ - w} dw \pm \pi i h(c_+) = \int_{C_b^{\text{ext}}} \frac{h(w)}{c_+ - w} dw. \quad (56)$$

Here the last equality follows from the fact $h(c_+) = 0$. Therefore, $I_1 = \Theta(1)$ as $z \rightarrow c_+$ as well. Hence, we see that

$$\int_{-1}^1 \frac{\gamma_b(s, t)}{z - \zeta(s, t)} ds = \begin{cases} \Theta(\log(c_+ - z)) & \text{as } z \rightarrow c_+, \text{ if } \gamma_b(1, t) \neq 0. \\ \Theta(1) & \text{as } z \rightarrow c_+, \text{ if } \gamma_b(1, t) = 0. \end{cases} \quad (57)$$

In fact, this shows that near the $+$ edge, we may find bounded function Φ_{\pm} holomorphic away from the body such that

$$\int_{-1}^1 \frac{\gamma_b(s, t)}{z - \zeta(s, t)} ds = \Phi_+(z) - g(c_+) \log(c_+ - z) - \nabla g(c_+) \cdot ((z - c_{\pm}) (\log(c_{\pm} - z))). \quad (58)$$

A similar equation holds at the $-$ edge with signs reversed.

B Log quadrature with blob regularization

Here, we describe briefly how the log quadrature rule (42) can be modified to obtain (43). This quadrature rule is used in both the velocity smoothed Birkhoff-Rott (48) and pressure-jump equations (49). Like in section 3.3.1, we proceed by assuming that the position of the free vortex sheet is given as a piecewise linear function of circulation. This assumption allows us to compute the integral analytically on each subinterval before summing the contributions. More explicitly, suppose that we have k_{\pm} points on the \pm sheet. Denote their positions $\zeta_{\pm,j}$ and their corresponding circulations by $\Gamma_{\pm,j}$ then we have that

$$\begin{aligned} \int_0^{\Gamma_{\pm}(t)} \frac{\overline{z - \zeta_{\pm}(\Gamma', t)}}{|z - \zeta_{\pm}(\Gamma', t)|^2 + \delta^2} d\Gamma' &= \sum_{j=0}^{k_{\pm}} \int_{\Gamma_{\pm,j}}^{\Gamma_{\pm,j+1}} \frac{\overline{z - \zeta_{\pm}(\Gamma', t)}}{|z - \zeta_{\pm}(\Gamma', t)|^2 + \delta^2} d\Gamma' \\ &\approx - \sum_{j=0}^{k_{\pm}} \int_{\Gamma_{\pm,j}}^{\Gamma_{\pm,j+1}} \frac{\overline{a_j \Gamma' + b_j - z}}{|a_j \Gamma' + b_j - z|^2 + \delta^2} d\Gamma' \\ &= \sum_{j=0}^{k_{\pm}} \frac{-1}{a_j} \int_{\Gamma_{\pm,j}}^{\Gamma_{\pm,j+1}} \frac{\overline{\Gamma' - c_j}}{|\Gamma' - c_j|^2 + \delta^2} d\Gamma'. \end{aligned}$$

Here, $c_j = \frac{z - b_j}{a_j}$, and a_j, b_j are given as before. Let $c_j^R = \Re c_j$ and $c_j^I = \Im c_j$ so that $c_j = c_j^R + i c_j^I$. By splitting the integrand into real and imaginary parts,

$$\frac{\overline{\Gamma' - c_j}}{|\Gamma' - c_j|^2 + \delta^2} d\Gamma' = \frac{\Gamma' - c_j^R}{|\Gamma' - c_j|^2 + \delta^2} d\Gamma' + i \frac{c_j^I}{|\Gamma' - c_j|^2 + \delta^2} d\Gamma', \quad (59)$$

it is easy to compute that

$$\begin{aligned} \int_{\Gamma_{\pm,j}}^{\Gamma_{\pm,j+1}} \frac{\overline{\Gamma' - c_j}}{|\Gamma' - c_j|^2 + \delta^2} d\Gamma' &= \frac{1}{2} \log \frac{(\Gamma_{\pm,j+1} - c_j^R)^2 + (c_j^I)^2 + \delta^2}{(\Gamma_{\pm,j} - c_j^R)^2 + (c_j^I)^2 + \delta^2} \\ &\quad + \frac{i c_j^I}{\sqrt{(c_j^I)^2 + \delta^2}} \left(\arctan \left(\frac{\Gamma_{\pm,j+1} - c_j^R}{\sqrt{(c_j^I)^2 + \delta^2}} \right) - \arctan \left(\frac{\Gamma_{\pm,j} - c_j^R}{\sqrt{(c_j^I)^2 + \delta^2}} \right) \right). \end{aligned} \quad (60)$$

Hence, the contributions to the conjugate fluid velocity given by the free sheets can be approximated by the formula

$$\begin{aligned} \frac{1}{2\pi i} \int_0^{\Gamma_{\pm}(t)} \frac{\overline{z - \zeta_{\pm}(\Gamma', t)}}{|z - \zeta_{\pm}(\Gamma', t)|^2 + \delta^2} d\Gamma' &\approx \sum_{j=0}^{k_{\pm}} \frac{-1}{a_j 2\pi i} \left(\frac{1}{2} \log \left(\frac{(\Gamma_{\pm,j+1} - c_j^R)^2 + (c_j^I)^2 + \delta^2}{(\Gamma_{\pm,j} - c_j^R)^2 + (c_j^I)^2 + \delta^2} \right) \right. \\ &\quad \left. + \frac{i c_j^I}{(c_j^I)^2 + \delta^2} \left(\arctan \left(\frac{\Gamma_{\pm,j+1} - c_j^R}{\sqrt{(c_j^I)^2 + \delta^2}} \right) - \arctan \left(\frac{\Gamma_{\pm,j} - c_j^R}{\sqrt{(c_j^I)^2 + \delta^2}} \right) \right) \right). \end{aligned} \quad (61)$$

C Numerical parameters and grid refinement studies

Here we summarize the numerical parameters used to obtain the results in the main body of the paper.

Time step, dt	0.012
Number of grid points on the body, n	100
Number of grid points on the free sheets in the far field, k_{\pm}	1000

Table 5: Summary of the numerical parameters used in the main results of the paper.

Here, the far field refers to the portions of the \pm sheets that have arc-length distances from the edges *greater* than 20 (i.e. 10 times the plate length). Similarly, the near field is defined as the portions of the \pm sheets that have arc-length distances from the edges *less* than 20. To ensure the far-field portions of the free sheets contain at most k_{\pm} points, we perform the following sheet pruning procedure. At the end of each time step, for each point in the far field, we compute the change in velocity on the body incurred by removing said grid point using equation (13). The grid point that incurs the smallest change in velocity when removed is then deleted. This procedure is iterated until the total number of points in the far field is equal to k_{\pm} . A similar criterion for point deletion was used in [AMP13]. The log quadrature rule described in section 3.3.1 and appendix B is used only to compute the velocity induced by the near field, while the usual trapezoidal rule is used to compute the velocity induced by the far field. Hence, while the near field is treated as a vortex sheet, the far field is treated more as a collection of point vortices. Typically, the near field is represented with between 250 and 500 points with $dt = 0.012$, but this number increases as the time step size decreases.

Formally, the algorithm is at least second order in both time and space. However, as figure 27 shows, the order of convergence as $dt \rightarrow 0$ is at worst ≈ 1.24 for the range of R_1 considered. The order of convergence in $\frac{1}{n}$ as the number of grid points $n \rightarrow \infty$ is ≈ 2 . These estimates were obtained via linear regression in logarithmic coordinates. The second-order convergence in the number of body grid points is expected, since when computing the strength γ_b , the trapezoidal rule is used on the Chebyshev grid which is second order in the number of body grid points. Indeed, since the Chebyshev grid is obtained by applying the function $-\cos(x)$ to the uniform grid with n points on the interval $[0, \pi]$, the error incurred from the trapezoidal rule is $\sum_{k=0}^n O(|\cos(k\pi/n) - \cos((k+1)\pi/n)|^3) = 1/n^3 \sum_{k=0}^n O(|\sin(k\pi/n)|^3) = O(1/n^2)$. This is because although the Chebyshev grid mesh size is of size $O(1/n^2)$ near the edges of the plate, the error contributed by the segments near the center of the plate with mesh size $O(1/n)$ dominates.

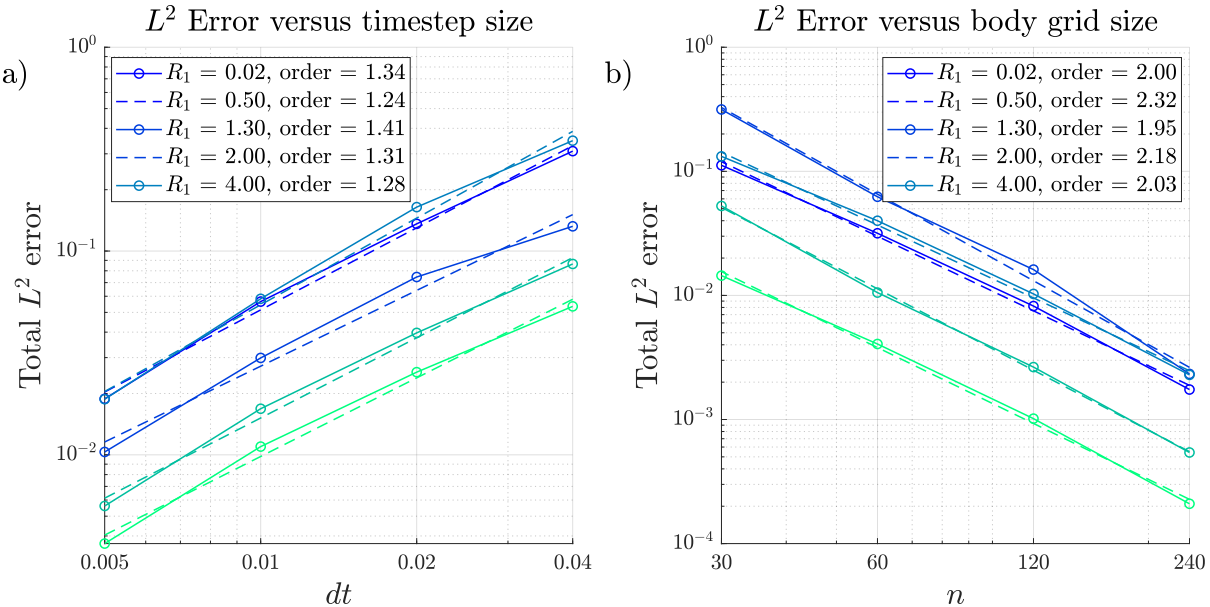


Figure 27: Convergence studies of the discretization parameters dt (panel a), and n (panel b) for the flat plate and various values of R_1 . The total L^2 error of the plate trajectory and angle up to time $t_{\text{final}} = 10$ is plotted, and for each $R_1 = 0.02, 0.5, 1.3, 2, 4$, the corresponding best-fit power law is plotted with dashed lines. Here the error is the difference with respect to the solution with $dt = 0.0025$ and $n = 480$.

The convergence study in figure 27 was limited only to short times. Indeed, as noted in [Are83], the motion of two-dimensional vortex structures is inherently chaotic, in the sense that it is highly sensitive to initial conditions. For any chaotic dynamical system, any change to numerical parameters, including grid refinement, can dramatically affect the computed motions of the free vortex sheets over long times. The motion of the plate, being coupled to the chaotic motion of the free vortex sheets, is chaotic as well. Due to the chaotic nature of the system, the error grows exponentially over long times. In figures 28, 29, and 30 below, we instead consider how the large-scale qualitative features of simulation change under grid refinement. For illustration, we once again focus only on the flat plate. In all cases observed, only when tumbling occurs the system is not chaotic ($R_1 = 1.3$). This is likely because the tumbling motion exhibits the most regular vortex wake, as can be seen from figure 10.

C.1 Refinement of the time step dt

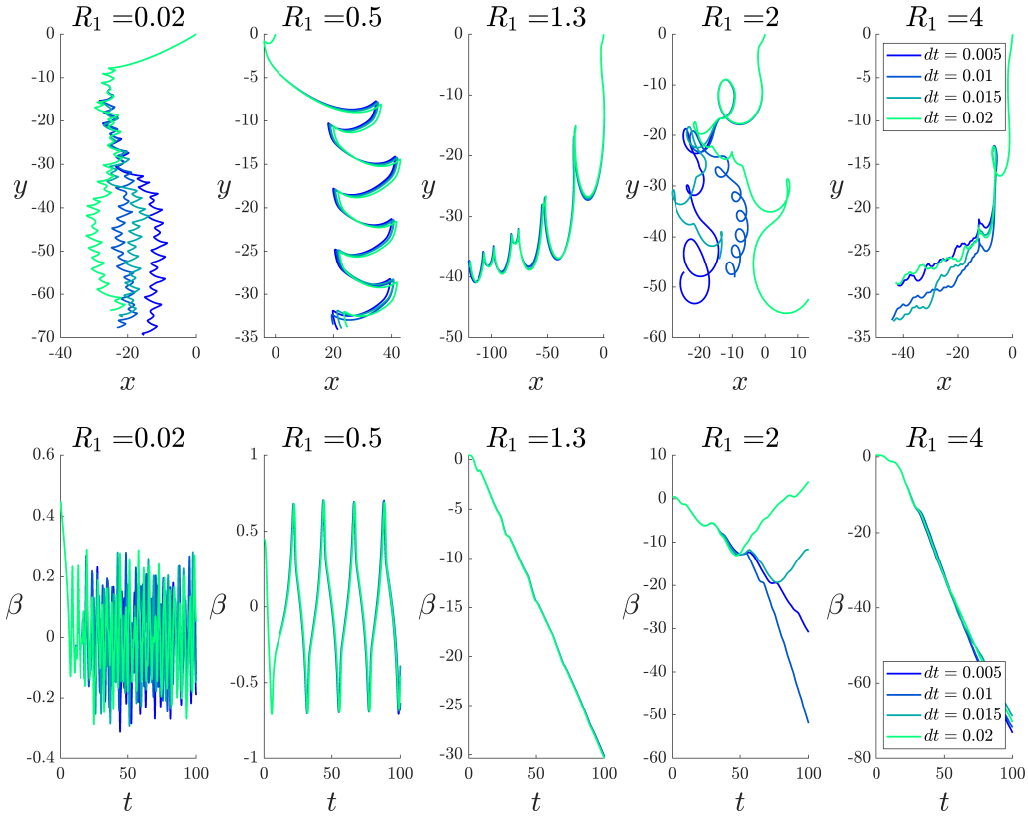


Figure 28: The center-of-mass trajectories $\zeta_G(t)$ (top row) and the orientation angle $\beta(t)$ (bottom row) for $dt = 0.005, 0.01, 0.015, 0.02$ for the flat plate with $R_1 = 0.02, 0.5, 1.3, 2, 4$ up to $t = 100$. Here, $n = 100, k_{\pm} = 1000$. For all $dt \leq 0.02$ the qualitative dynamics exhibited are nearly identical. While the initial trajectories overlap, for all R_1 outside the tumbling regime, the trajectories deviate from one another at an exponential rate.

C.2 Refinement in the number of body grid points, n

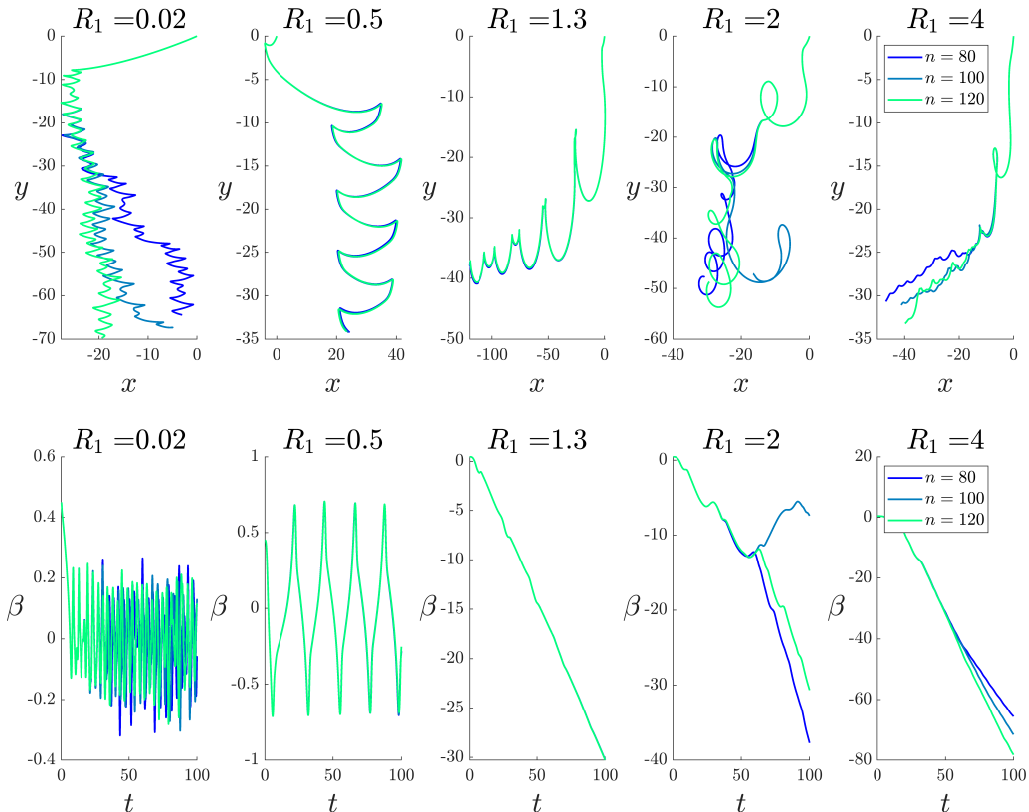


Figure 29: The center-of-mass trajectories $\zeta_G(t)$ (top row) and the orientation angle $\beta(t)$ (bottom row) for $n = 80, 100, 120$ for the flat plate with $R_1 = 0.02, 0.5, 1.3, 2, 4$ until $t = 100$. Here, $dt = 0.01, k_{\pm} = 1000$. For all $n \geq 80$ the qualitative dynamics exhibited are nearly identical. While the initial trajectories overlap, for all R_1 outside the tumbling regime, the trajectories deviate from one another at an exponential rate.

C.3 Refinement in the number of vortex sheet grid points in the far field, k_{\pm}

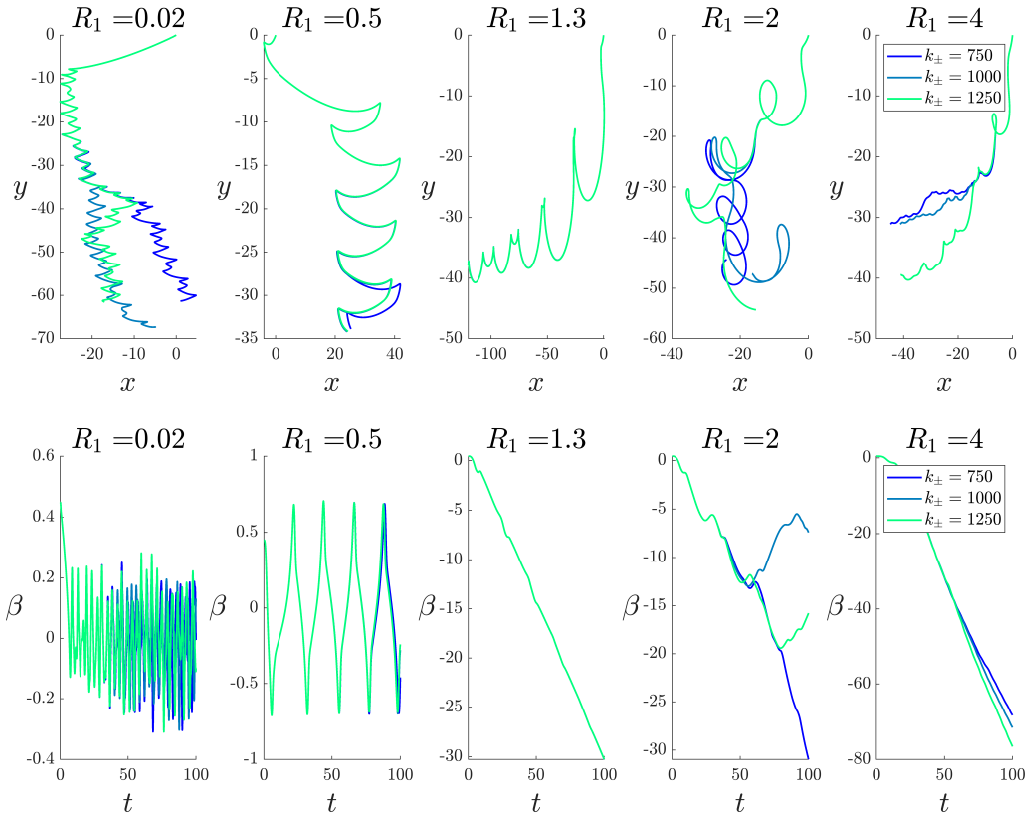


Figure 30: The center-of-mass trajectories $\zeta_G(t)$ (top row) and the orientation angle $\beta(t)$ (bottom row) for $k_{\pm} = 750, 1000, 1250$ for the flat plate with $R_1 = 0.02, 0.5, 1.3, 2, 4$ until $t = 100$. Here, $dt = 0.01$, $n = 100$. For all $n \geq 80$ the qualitative dynamics exhibited are nearly identical. While the initial trajectories overlap, for all R_1 outside the tumbling regime, the trajectories deviate from one another at an exponential rate.

References

- [Mus58] N. I. Muskhelishvili. “Singular integral equations; boundary problems of functions theory and their applications to mathematical physics”. In: (1958).
- [HJR66] R. M. Halleen, J. P. Johnston, and W. C. Reynolds. “The Laminar Boundary Layer on a Rotating Circular Arc Blade”. In: *Journal of Basic Engineering* 88.1 (Mar. 1966), pp. 111–120. ISSN: 0021-9223. DOI: [10.1115/1.3645782](https://doi.org/10.1115/1.3645782). eprint: https://asmedigitalcollection.asme.org/fluidseengineering/article-pdf/88/1/111/5764309/111_1.pdf. URL: <https://doi.org/10.1115/1.3645782>.
- [Bat67] G. K. Batchelor. *An introduction to fluid dynamics*. Cambridge university press, 1967.
- [Smi71] EH Smith. “Autorotating wings: an experimental investigation”. In: *Journal of Fluid Mechanics* 50.3 (1971), pp. 513–534.
- [Did79] Norbert Didden. “On the formation of vortex rings: Rolling-up and production of circulation”. In: *Zeitschrift für angewandte Mathematik und Physik ZAMP* 30.1 (Jan. 1, 1979), pp. 101–116. DOI: [10.1007/BF01597484](https://doi.org/10.1007/BF01597484). URL: <https://doi.org/10.1007/BF01597484>.
- [Moo79] Derek William Moore. “The spontaneous appearance of a singularity in the shape of an evolving vortex sheet”. In: *Proceedings of the Royal Society of London. A. Mathematical and Physical Sciences* 365.1720 (1979), pp. 105–119.
- [Are83] Hassan Aref. “Integrable, chaotic, and turbulent vortex motion in two-dimensional flows”. In: *Annual review of fluid mechanics* 15 (1983), pp. 345–389.
- [Kra86a] Robert Krasny. “A study of singularity formation in a vortex sheet by the point-vortex approximation”. In: *Journal of Fluid Mechanics* 167 (1986), pp. 65–93. DOI: [10.1017/S0022112086002732](https://doi.org/10.1017/S0022112086002732).
- [Kra86b] Robert Krasny. “Desingularization of periodic vortex sheet roll-up”. In: *Journal of Computational Physics* 65.2 (1986), pp. 292–313.
- [Gol90] Michael A. Golberg. “Introduction to the Numerical Solution of Cauchy Singular Integral Equations”. In: 1990. URL: <https://api.semanticscholar.org/CorpusID:118863621>.
- [Kra90] Robert Krasny. “Computing vortex sheet motion”. In: *Proc. of Inte. Cong. Math., Kyoto, Japan*. 1990, pp. 1573–1583.
- [She92] M. J. Shelley. “A study of singularity formation in vortex-sheet motion by a spectrally accurate vortex method”. In: *Journal of Fluid Mechanics* 244 (1992), pp. 493–526. DOI: [10.1017/S0022112092003161](https://doi.org/10.1017/S0022112092003161).
- [KL93] Petros Koumoutsakos and Anthony Leonard. “Direct numerical simulations using vortex methods”. In: *Vortex flows and related numerical methods*. Springer, 1993, pp. 179–190.

[NK94] Monika Nitsche and Robert Krasny. “A numerical study of vortex ring formation at the edge of a circular tube”. In: *Journal of Fluid Mechanics* 276 (1994), pp. 139–161.

[Fie+97] Stuart B. Field et al. “Chaotic dynamics of falling disks”. In: *Nature* 388.6639 (July 1997), pp. 252–254. ISSN: 1476-4687. DOI: [10.1038/40817](https://doi.org/10.1038/40817). URL: <https://doi.org/10.1038/40817>.

[BEM98] Andrew Belmonte, Hagai Eisenberg, and Elisha Moses. “From flutter to tumble: inertial drag and Froude similarity in falling paper”. In: *Physical Review Letters* 81.2 (1998), p. 345.

[Boi01] IV Boikov. “Numerical methods of computation of singular and hypersingular integrals”. In: *International Journal of Mathematics and Mathematical Sciences* 28.3 (2001), pp. 127–179.

[TT01] ADRIAN L.R. THOMAS and GRAHAM K. TAYLOR. “Animal Flight Dynamics I. Stability in Gliding Flight”. In: *Journal of Theoretical Biology* 212.3 (2001), pp. 399–424. ISSN: 0022-5193. DOI: <https://doi.org/10.1006/jtbi.2001.2387>. URL: <https://www.sciencedirect.com/science/article/pii/S0022519301923872>.

[Jon03] Marvin A. Jones. “The separated flow of an inviscid fluid around a moving flat plate”. In: *Journal of Fluid Mechanics* 496 (2003), pp. 405–441. URL: <https://api.semanticscholar.org/CorpusID:120292659>.

[PW04] Umberto Pesavento and Z Jane Wang. “Falling paper: Navier-Stokes solutions, model of fluid forces, and center of mass elevation”. In: *Physical review letters* 93.14 (2004), p. 144501.

[APW05a] A Andersen, U Pesavento, and Z Jane Wang. “Unsteady aerodynamics of fluttering and tumbling plates”. In: *Journal of Fluid Mechanics* 541 (2005), pp. 65–90.

[APW05b] A. ANDERSEN, U. PESAVENTO, and Z. JANE WANG. “Analysis of transitions between fluttering, tumbling and steady descent of falling cards”. In: *Journal of Fluid Mechanics* 541 (2005), pp. 91–104. DOI: [10.1017/S0022112005005847](https://doi.org/10.1017/S0022112005005847).

[JS05] Marvin A Jones and Michael J Shelley. “Falling cards”. In: *Journal of Fluid Mechanics* 540 (2005), pp. 393–425.

[CVZ06] Stephen Childress, Nicolas Vandenberghe, and Jun Zhang. “Hovering of a passive body in an oscillating airflow”. In: *Physics of Fluids* 18.11 (Nov. 2006), p. 117103. ISSN: 1070-6631. DOI: [10.1063/1.2371123](https://doi.org/10.1063/1.2371123). eprint: <https://pubs.aip.org/aip/pof/article-pdf/doi/10.1063/1.2371123/16710876/117103\1\online.pdf>. URL: <https://doi.org/10.1063/1.2371123>.

[Alb09] Silas Alben. “Simulating the dynamics of flexible bodies and vortex sheets”. In: *Journal of Computational Physics* 228.7 (2009), pp. 2587–2603. ISSN: 0021-9991. DOI: <https://doi.org/10.1016/j.jcp.2008.12.020>. URL: <https://www.sciencedirect.com/science/article/pii/S0021999108006591>.

[ML09] Sébastien Michelin and Stefan G Llewellyn Smith. “An unsteady point vortex method for coupled fluid–solid problems”. In: *Theoretical and Computational Fluid Dynamics* 23 (2009), pp. 127–153.

[Alb10a] Silas Alben. “Flexible sheets falling in an inviscid fluid”. In: *Physics of Fluids* 22.6 (June 2010), p. 061901. ISSN: 1070-6631. DOI: [10.1063/1.3432128](https://doi.org/10.1063/1.3432128). eprint: <https://pubs.aip.org/aip/pof/article-pdf/doi/10.1063/1.3432128/16734676/061901\1\online.pdf>. URL: <https://doi.org/10.1063/1.3432128>.

[Alb10b] Silas Alben. “Regularizing a vortex sheet near a separation point”. In: *Journal of Computational Physics* 229.13 (2010), pp. 5280–5298. ISSN: 0021-9991. DOI: <https://doi.org/10.1016/j.jcp.2010.03.044>. URL: <https://www.sciencedirect.com/science/article/pii/S0021999110001634>.

[Tam+10] Daniel Tam et al. “Tumbling dynamics of passive flexible wings”. In: *Physical review letters* 104.18 (2010), p. 184504.

[ZCL11] Hongjie Zhong, Shiyi Chen, and Cunbiao Lee. “Experimental study of freely falling thin disks: Transition from planar zigzag to spiral”. In: *Physics of Fluids* 23.1 (2011).

[Alb12] Silas Alben. “The attraction between a flexible filament and a point vortex”. In: *Journal of Fluid Mechanics* 697 (2012), pp. 481–503. DOI: [10.1017/jfm.2012.78](https://doi.org/10.1017/jfm.2012.78).

[Alb+12] Silas Alben et al. “Dynamics of freely swimming flexible foils”. In: *Physics of Fluids* 24.5 (May 2012), p. 051901. ISSN: 1070-6631. DOI: [10.1063/1.4709477](https://doi.org/10.1063/1.4709477). eprint: <https://pubs.aip.org/aip/pof/article-pdf/doi/10.1063/1.4709477/14929326/051901\1\online.pdf>. URL: <https://doi.org/10.1063/1.4709477>.

[Pan+12] Yulin Pan et al. “Boundary-element method for the prediction of performance of flapping foils with leading-edge separation”. In: *Journal of Fluid Mechanics* 698 (2012), pp. 446–467. DOI: [10.1017/jfm.2012.119](https://doi.org/10.1017/jfm.2012.119).

[Ram+12] Kiran Kumar Ramesh et al. “Theoretical modeling of leading edge vortices using the leading edge suction parameter”. In: *30th AIAA Applied Aerodynamics Conference*. 2012, p. 3027.

[She+12] JX Sheng et al. “Simulating vortex wakes of flapping plates”. In: *Natural Locomotion in Fluids and on Surfaces: Swimming, Flying, and Sliding*. Springer. 2012, pp. 255–262.

[Alb13] Silas Alben. “Optimizing snake locomotion in the plane”. In: *Proceedings of the Royal Society A: Mathematical, Physical and Engineering Sciences* 469.2159 (2013), p. 20130236.

[AMP13] Silas Alben, LA Miller, and Jifeng Peng. “Efficient kinematics for jet-propelled swimming”. In: *Journal of Fluid Mechanics* 733 (2013), pp. 100–133.

[HNK14] Luke Heisinger, Paul Newton, and Eva Kanso. “Coins falling in water”. In: *Journal of fluid mechanics* 742 (2014), pp. 243–253.

[WL15] R.-J. Wu and S.-Y. Lin. “The Flow of A Falling Ellipse: Numerical Method and Classification”. In: *Journal of Mechanics* 31.6 (Aug. 2015), pp. 771–782. ISSN: 1811-8216. DOI: [10.1017/jmech.2015.47](https://doi.org/10.1017/jmech.2015.47). eprint: https://academic.oup.com/jom/article-pdf/31/6/771/34414961/jom_v31_6_771.pdf. URL: <https://doi.org/10.1017/jmech.2015.47>.

[HNK16] Yangyang Huang, Monika Nitsche, and Eva Kanso. “Hovering in oscillatory flows”. In: *Journal of Fluid Mechanics* 804 (2016), pp. 531–549. DOI: [10.1017/jfm.2016.535](https://doi.org/10.1017/jfm.2016.535).

[VSK16] Lionel Vincent, W Scott Shambaugh, and Eva Kanso. “Holes stabilize freely falling coins”. In: *Journal of Fluid Mechanics* 801 (2016), pp. 250–259.

[Wan+16] Y. Wang et al. “Numerical study on the freely falling plate: Effects of density ratio and thickness-to-length ratio”. In: *Physics of Fluids* 28.10 (Oct. 2016), p. 103603. ISSN: 1070-6631. DOI: [10.1063/1.4963242](https://doi.org/10.1063/1.4963242). eprint: https://pubs.aip.org/aip/pof/article-pdf/doi/10.1063/1.4963242/15853901/103603_1_online.pdf. URL: <https://doi.org/10.1063/1.4963242>.

[Cum+18] Cathal Cummins et al. “A separated vortex ring underlies the flight of the dandelion”. In: *Nature* 562.7727 (2018), pp. 414–418.

[Hua+18] Yangyang Huang et al. “Bistability in the rotational motion of rigid and flexible flyers”. In: *Journal of Fluid Mechanics* 849 (2018), pp. 1043–1067. DOI: [10.1017/jfm.2018.446](https://doi.org/10.1017/jfm.2018.446).

[Xia+18] Yang Xiang et al. “Trajectory modes and wake patterns of freely falling plates”. In: *Journal of Visualization* 21.3 (June 2018), pp. 433–441. ISSN: 1875-8975. DOI: [10.1007/s12650-017-0469-8](https://doi.org/10.1007/s12650-017-0469-8). URL: <https://doi.org/10.1007/s12650-017-0469-8>.

[Ami+19] Khunsa Amin et al. “The role of shape-dependent flight stability in the origin of oriented meteorites”. In: *Proceedings of the National Academy of Sciences* 116.33 (2019), pp. 16180–16185. DOI: [10.1073/pnas.1815133116](https://doi.org/10.1073/pnas.1815133116). eprint: <https://www.pnas.org/doi/pdf/10.1073/pnas.1815133116>. URL: <https://www.pnas.org/doi/abs/10.1073/pnas.1815133116>.

[Eld19] Jeff Eldredge. *Mathematical Modeling of Unsteady Inviscid Flows*. Aug. 2019. ISBN: 978-3-030-18319-6. DOI: [10.1007/978-3-030-18319-6](https://doi.org/10.1007/978-3-030-18319-6).

[Led+19] Pier Giuseppe Ledda et al. “Flow dynamics of a dandelion pappus: A linear stability approach”. In: *Physical review fluids* 4.7 (2019), p. 071901.

[KD20] Vivek Kr. Kushwaha and Arnab K. De. “Aerodynamics of multiple freely falling plates”. In: *Physics of Fluids* 32.10 (Oct. 2020), p. 103603. ISSN: 1070-6631. DOI: [10.1063/5.0021794](https://doi.org/10.1063/5.0021794). eprint: https://pubs.aip.org/aip/pof/article-pdf/doi/10.1063/5.0021794/15660400/103603_1_online.pdf. URL: <https://doi.org/10.1063/5.0021794>.

[MA20] C. Mavroyiakoumou and S. Alben. “Large-amplitude membrane flutter in inviscid flow”. In: *Journal of Fluid Mechanics* 891 (2020), A23. DOI: [10.1017/jfm.2020.153](https://doi.org/10.1017/jfm.2020.153).

[RKD20] A. Rana, V. K. Kushwaha, and Arnab Kumar De. “A numerical study on the effect of aspect-ratio and density ratio on the dynamics of freely falling plate in the flutter-to-tumble transition regime”. In: *Sādhanā* 45.1 (Oct. 2020), p. 259. ISSN: 0973-7677. DOI: [10.1007/s12046-020-01487-y](https://doi.org/10.1007/s12046-020-01487-y). URL: <https://doi.org/10.1007/s12046-020-01487-y>.

[Kim+21] Bong Hoon Kim et al. “Three-dimensional electronic microfliers inspired by wind-dispersed seeds”. In: *Nature* 597.7877 (Sept. 1, 2021), pp. 503–510. DOI: [10.1038/s41586-021-03847-y](https://doi.org/10.1038/s41586-021-03847-y). URL: <https://doi.org/10.1038/s41586-021-03847-y>.

[Nit21] Monika Nitsche. “Evaluation of near-singular integrals with application to vortex sheet flow”. In: *Theoretical and Computational Fluid Dynamics* 35.5 (Oct. 1, 2021), pp. 581–608. DOI: [10.1007/s00162-021-00577-9](https://doi.org/10.1007/s00162-021-00577-9). URL: <https://doi.org/10.1007/s00162-021-00577-9>.

[Li+22] Huilin Li et al. “Centre of mass location, flight modes, stability and dynamic modelling of gliders”. In: *Journal of Fluid Mechanics* 937 (2022), A6. DOI: [10.1017/jfm.2022.89](https://doi.org/10.1017/jfm.2022.89).

[Nar+23] Shreyas Narsipur et al. “Discrete vortex modeling of perching and hovering maneuvers”. In: *Theoretical and Computational Fluid Dynamics* 37.4 (2023), pp. 445–464.

[PR24] Olivia Pomerenk and Leif Ristrop. *Aerodynamic equilibria and flight stability of plates at intermediate Reynolds numbers*. 2024. arXiv: [2408.08864 \[physics.flu-dyn\]](https://arxiv.org/abs/2408.08864). URL: <https://arxiv.org/abs/2408.08864>.

[Soh24] Sung-Ik Sohn. “Simulation of the unsteady vortical flow of freely falling plates”. In: *Theoretical and Computational Fluid Dynamics* (Feb. 2024), pp. 1–21. DOI: [10.1007/s00162-024-00686-1](https://doi.org/10.1007/s00162-024-00686-1).